國 立 交 通 大 學

光電工程研究所

博士論文

微聚焦端泵浦摻釹釩酸釔雷射在簡併共振腔下的動態與穩態行為

Dynamics and stability behaviors in tightly focused end-pumped Nd:YVO_4 laser around the degenerate cavity configurations

研 究 生 ： 戴伯澤

指導教授 ： 謝文峰 教授

吳小華 教授

中 華 民 國 九 十 四 年 六 月

微聚焦端泵浦摻釹釩酸釔雷射在簡併共振腔下的動態與穩態行為

Dynamics and stability behaviors in tightly focused end-pumped Nd:YVO_4 laser around the degenerate cavity configurations

研 究 生: 戴伯澤　　Student: Po-Tse Tai

指導教授: 謝文峰　　Advisor: Wen-Feng Hsieh

吳小華　　Hsiao-Hua Wu

國 立 交 通 大 學

光電工程研究所

博 士 論 文

A Thesis

Submitted to the Department of Photonics & Institute of Electro-Optical Engineering

College of Electrical Engineering and Computer Science

National Chiao Tung University

in partial Fulfillment of Requirements

for the Degree of

Doctor of philosophy

in

Electro-Optical Engineering

June 2005

Hsinchu, Taiwan, Republic of China

中華民國九十四年六月

誌 謝

從小到大的求學歷程中，只有攻讀博士的階段不知道是否可以或是何時可以畢業。在這一段漫長的過程中，所得到的經驗是非常寶貴的。學位的取得不只是帶來喜悅而且也帶來了自我的肯定，這些心境的改變勢必會在往後的日子慢慢的醞釀。

在這段期間非常感謝指導老師謝文峰教授在研究態度與精神上的鍛鍊，以及吳小華教授在實驗技巧上的指導，使我能夠具備該有的技能。也非常感謝與我合作非常密切的陳慶緒學長，因為數值模型的建立使得我的實驗能有更完善的解釋。對於兩個跟我一起做實驗的學弟李國昶與邱偉豪，也非常感謝你們的努力讓我有多餘的時間，可以擴展實驗的方向與技巧，在這也祝福你們有美好的將來。幸運的在我博士班最後的兩年半讓我遇到了珮芳。使我在低潮的時候能夠樂觀的面對，遇到瓶頸時能夠給我突破的靈感。最重要的，妳也能夠和我一起分享生命裡的喜悅，希望我們能夠永遠的扶持對方下去。感謝這段期間遇到的所有人，你們給了我一個難忘的回憶。

感謝國科會計畫NSC93-2112-M-009-035 所提供的獎學金以及實驗的經費讓我能夠順利的完成所有的研究。

微聚焦端泵浦摻釹釩酸釔雷射在簡併共振腔下的動態與穩態行爲

學生: 戴伯澤　　指導老師: 謝文峰 教授

吳小華 教授

國立交通大學光電工程學系

摘要

我們研究一個操作在 1/3 簡併共振腔附近與小聚焦端泵浦的摻釹釩酸釔雷射，其共振腔結構相關的動態行爲。強烈聚焦的泵浦光線會因爲熱透鏡的效果，而產生巨大的相位變化進而影響共振腔的結構。爲了讓數值模擬能夠符合實驗的結果，我們將熱透鏡的效應加入數值模擬。數值模擬可以指出哪些位置可以產生自脈衝的現象，爲什麼我們可以在長短不同共振腔下觀察到時-空不穩脈衝現象，以及只有時間不穩定脈衝，這些結果都跟實驗非常的符合。除了在長腔的不穩區域之外，我們實驗上也觀察到橫模的光頻鎖定，及無橫模拍頻。利用基因演算法計算模態展開時，每個模態的振幅權重以及相對的相位，我們發現在完全簡併的共振腔下所有的橫模都是同相位。即使我們調離開簡併共振腔，所有的橫模還是保有相位與光頻的鎖定。即便調離簡併共振腔大約 1mm，我們仍可以觀察到模形(beam profile)會隨著傳播方向改變 ，這是由於所有的橫模在一開始就是相位鎖定。

由於在簡併共振腔下所有的橫模會保有光頻與相位的鎖定，我們可以利用這個特性來控制雷射的模形。我們驗證了在一個小聚焦與端泵浦的摻釹釩酸釔雷射可以直接產生多樣的瓶型光束。只要適當的控制泵浦

光斑與腔內實光欄的大小，在半共焦腔、1/3 簡併腔、與 1/5 簡併腔下可以產生不同但是對比度極佳的瓶型光束。這樣的新發現是適用於內含任意增益介質之小聚焦端泵浦雷射。

這樣的雷射也可抑制空間燒洞(spatial hole burning)效應。由於雷射模會自動調整大小以符合泵浦光斑，雷射可以在被幫浦增益介質區域內達到很高的光強度，而使得大部分的增益被高強度的駐波消耗掉。我們利用一個縱向相關的速率方程式來描述與研究這個在平凹共振腔摻釹釩酸釔雷射的實驗。即使高於 20 倍的閥值，實驗上我們可發現這個抑制空間燒洞的效應。

Dynamics and stability behaviors in tightly focused end-pumped Nd:YVO_4 laser around the degenerate cavity configurations

Student: Po-Tse Tai

Advisor: Professor Wen-Feng Hsieh
Professor Hsiao-Hua Wu

Department of Photonics and Institute of Electro-Optical Engineering
National Chiao Tung University

Abstract

We experimentally and numerically studied cavity-dependence of laser dynamics in an tightly-focused end-pumped Nd:YVO_4 laser which operates in the vicinity of 1/3-degenerate cavity. The tightly-focused pump beam results in enormous phase distortion which influences the cavity configuration through the thermal lens effect, therefore, the thermal lens effect is considered in our simulation. The simulation results well explain our experimental observation including the regions of self-pulsation, the reasons why we should observe the temporal or the spatiotemporal dynamics in the instability region on short- or long-cavity side of the degeneracy, and the influence of thermal lens. In addition, the transverse modes are all frequency-locked over the cavity tuning except for the instability regions. By decomposing the calculated mode (similar to the observed one) into the degenerate transverse modes to obtain their mode weights and relative phases, we found that the transverse modes are all in phase at the exactly degenerate cavity. Except for the cavity configuration within the instability

region on the long cavity side, all of the transverse modes are phase- and frequency-locked to one another even when the cavity is tuned away from the degeneracy. This finding consists with the experimental observation that the stationary transverse mode pattern does vary along the propagation axis due to interfere of Guoy phases from the phase-locked transverse modes even for cavity length being adjusted 1mm away from the degeneracy.

Because the transverse modes which govern the laser pattern are in-phase and frequency-locked at the degeneracy, we should be able to control the laser pattern. We demonstrate various optical bottle beams can be directly generated from a tightly focused end-pumped Nd:YVO_4 laser. By controlling the size of pump beam and inserting an intracavity aperture in the plano-concave cavity, we obtain good contrast optical bottles at semi-confocal, 1/3-, and 1/5-degenerate cavity configurations, respectively. This new observation is universal that is suitable for any kinds of gain media in tightly end-pumped lasers.

We also found that the spatial hole-burning effect can be suppressed in this laser. Due to shrinkage of the beam waist of laser mode to match the pump beam, this laser can attain very high intensity in the pump region of gain medium and therefore most of its gain is depleted even by a standing wave. This was demonstrated by a simulation with spatial dependent rate equations and experiment results of a plano-concave Nd:YVO_4 laser. The suppression effect was observed up to 20 times the pump threshold.

Table of contents

List of Figures

Chapter 1 Introduction

A laser system must contain a pumping source, gain media, and optical resonator. The simplest kind of optical resonator consists of just two curved mirrors set up facing to each other. Simple two-mirror cavities are widely used in practical lasers, and the properties of stable resonators are the basic lore of laser physics. Although the paraxial optics can easily obtain a geometrical stable condition, there are many dynamics and stability behaviors in some special cavity configurations [1-7]. In this study, we will focus on laser dynamics and stationary laser parameters dependent on its resonators.

1.1 Geometrical stable condition

Gaussian beams are the eigenfunctions of a laser resonator. We can use a complex q-parameter to represent a Gaussian beam of which the real and the imaginary parts respectively indicate the radius of curvature and the beam width. The transformation rule of paraxial wave using the ABCD matrix elements to relate the q-parameters as it propagates according to the so-called ABCD law as

$$q_2 = \frac{Aq_1 + B}{Cq_1 + D}, \tag{1.1}$$

where q_1 is the initial state of Gaussian beam and q_2 is the final state after Gaussian beam propagates through a paraxial optical system characterized by the ABCD matrix. Let the elements of ABCD matrix in Eq. (1.1) be those for a round trip of the laser cavity. Thus, q_1 will equal to q_2 because the

laser beam should be self-consistent after propagating a round trip. Therefore we can solve the self-consitent q-parameter q_s as

$$q_s = \frac{\left[-\frac{A-D}{2} \pm i\sqrt{1-\left(\frac{A+D}{2}\right)^2} \right]}{B}. \tag{1.2}$$

For ensuring q_s be a complex number, we obtain the criterion of a stable cavity:

$$\left|\frac{A+D}{2}\right| \le 1. \tag{1.3}$$

Assume two mirrors which form a resonator having radii of curvature of R_1 and R_2 are separated by L, the round trip elements of ABCD matrix are trivial to obtain and substitute into Eq. (1.3) and the stable condition of optical resonator becomes

$$0 \le g_1 g_2 \le 1, \tag{1.4}$$

where $g_{1,2} = 1 - L/R_{1,2}$. This stability criterion of Eq. (1.4) is suitable for any two-mirror optical resonator and is called the geometrically stable condition. However, we only consider the geometrically stable condition for a real laser cavity is not enough if there are additional effects that can result in instability output of laser, and we will discuss it as follows.

1.2 Degenerate cavities and iterative map

1.2-1 Resonance frequencies and degenerate cavities

The resonance condition for a standing-wave cavity is that the phase shift for total round-trip must be an integer multiple of 2π. The total phase shift from one end of cavity to the other end includes *k*L and Gouy phase

shift terms, where $k = 2\pi/\lambda$ is the wave number, λ is wavelength of laser, and the Gouy phase is an additional phase introduced by a paraxial wave function substitution for an (n,m)-th order Hermite-Gaussian mode in mathematics. The total Gouy phase shift of a laser cavity with resonator length L is given in terms of the *g*-parameters by the formula

$$(n+m+1)\cos^{-1}(\pm\sqrt{g_1 g_2}), \tag{1.5}$$

where n and m are the mode numbers in the x- and y-axes, respectively. Because the Gouy phase shift depends on Hermite-Gaussian mode number, different transverse modes of a stable Gaussian resonator have different resonance frequencies and the resonance frequency of Hermite-Gaussian (n,m) mode is therefore given by

$$\nu_{n,m,q} = \frac{c}{2L}\left(q + \frac{m+n+1}{\pi}\cos^{-1}\sqrt{g_1 g_2}\right), \tag{1.6}$$

where *q* is the longitudinal mode number. Form Eq. (1.6), we can define $\nu_l = c/2L$ is the longitudinal mode spacing, and $\nu_t = (\nu_l/\pi)\arccos[(g_1 g_2)^{1/2}]$ is the transverse mode spacing. The configurations with $g_1 g_2 = 0$, 1/4, and 1/2 correspond to $\nu_t/\nu_l = 1/2$, 1/3, and 1/4, respectively, therefore, we denote them as 1/2-, 1/3-, 1/4-degenerate configurations. In these configurations, the fundamental modes may be degenerate with other high-order transverse modes which obey Eq. (1.6). The degenerate modes may through the mode competition or the mode beating result in instability of laser output [8-9]. Therefore, we know the degenerate cavity is a good choice to investigate laser dynamics.

1.2-2 Iterative map

The iterative map is a mathematical tool to realize the dynamic behaviors in a physical system. This method use discrete time system to study a continuous system. Applying the ABCD matrix for a lossless two-mirror resonator, we can define a two-dimension iterative map which contains the spot size w and radius of curvature R as below [2]

$$\begin{cases} w_{n+1} = h(R_n, w_n) = w_n \sqrt{\left(A + B/R_n\right)^2 + \left(\lambda/\pi w_n^2\right)^2 B^2} \\ R_{n+1} = f(R_n, w_n) = \dfrac{\left(A + B/R_n\right)^2 + \left(\lambda/\pi w_n^2\right)^2 B^2}{\left(A + B/R_n\right)\left(C + D/R_n\right) + \left(\lambda/\pi w_n^2\right)^2 BD} \end{cases} . \qquad (1.7)$$

The suffix of n represents the round-trip index where A, B, C, and D are elements of the round-trip matrix, and the discrete time interval of the map is equal to one round-trip time of the resonator. Under linear stability analysis, the stability of fixed point is determined by its Jacobian eigenvalue of the map. The fixed point is the self-consistent solution of q-parameter, i.e., the steady-state solution. Therefore discussing the Jacobin eigenvalue at fixed point is equivalent to determine the dynamic stability of laser resonator.

Because the map belongs to conserve system, the determinant of Jacobian matrix equals to unity and the eigenvalue of Jacobian matrix depend on its trace. For convenience, we use the residue to discuss the stability condition which is defined as

$$\text{Res} = \frac{1}{4}\left[2 - \text{Tr}(M_J)\right], \qquad (1.8)$$

where M_J is the Jacobian matrix and Tr(M_J) is its trace. When 0<Res<1, the eigenvalues are complex with unity magnitude and the system is stable,

whereas the system is unstable with either Res<0 or Res>1.

In the standing wave resonators with real round-trip transfer matrices, the curvature of laser beam must match the end mirrors. Therefore, by substituting the the trace of Jacobin derived from the round-trip transfer matrix into Eq. (1.8), we have the residue

$$\mathrm{Res} = 1 - \left(A + B/R_1 \right)^2 = 1 - (2G_1G_2 - 1)^2 . \tag{1.9}$$

Here we have defined $G_1=a-b/R_1$ and $G_2=c-d/R_2$ as the G-parameters for general optical resonators, and a, b, c, and d are the elements of transfer matrix of single pass between the two end mirrors. We can use G-parameters to discuss the stability of a multi-element resonator.

For simplicity, we discuss the stability by a two-mirror resonator. Thus the single pass transfer matrix is $\begin{bmatrix} 1 & L \\ 0 & 1 \end{bmatrix}$ and

$$\mathrm{Res} = 1 - (2g_1g_2 - 1)^2, \tag{1.10}$$

where $g_{1,2} = 1 - L/R_{1,2}$ and the definition of g-parameters are the same as in Eq. (1.4). From Eq. (1.10), we found that the residue is a function of g_1g_2 only. A plot of the diagram of residue versus g_1g_2 is presented in Fig. 1-1. Since the resonator is dynamically unstable for Res<0 or Res>1, in Fig. 1-1, one gets a region with $g_1g_2<0$ or $g_1g_2>1$. And the dynamic stable region with 0<Res<1 is also geometrically stable corresponding to $0<g_1g_2<1$. It is critical stable for Res=0 with $g_1g_2=0$ or $g_1g_2=1$. The stable region of residue theorem is the same as the geometrical stability ones which has been discussed in Section 1.1. However, another critical stable point at $g_1g_2=1/2$ with Res=1 in Fig. 1-1 can not be found by using the paraxial optics.

Stability region decided by the iterative map of the beam parameters provides not only geometrical stable condition but also dynamically critical stable condition.

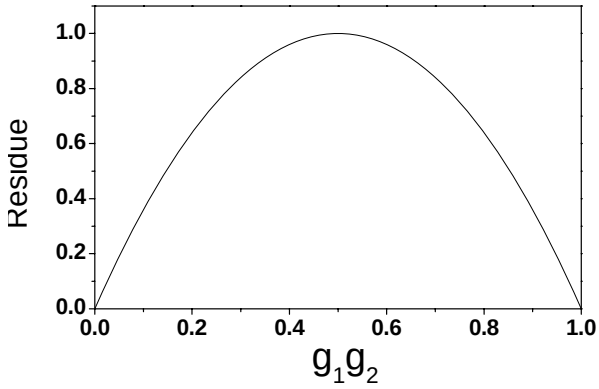

Fig. 1-1 The diagram of residue versus g_1g_2. It can easily be observed that the stable region of the residue is the same as geometrical stable condition.

From the residue theorem, these special cases with Res = 0, 1, 3/4, and 1/2 correspond to the low-order resonance where p=1, 2, 3, and 4 satisfying $\chi^p=1$, respectively. Here χ is the eigenvalue of M_J. Under these circumstances, the complicated dynamics may occur at these configurations if there is a persistent nonlinear effect. These special conditions correspond to $g_1g_2=0$ or $g_1g_2=1$ for Res=0; $g_1g_2=1/2$ for Res=1; $g_1g_2=1/4$ or $g_1g_2=3/4$ for Res=3/4; and $g_1g_2=\left(2\pm\sqrt{2}\right)/4$ for Res=1/2, respectively [1-2]. It is worth noting that these configurations correspond to degenerate cavities and these degenerate cavities are very sensitive to any perturbation in the laser system. Therefore if any nonlinear effect is in a laser system, the laser will present various dynamics behavior. In the previous study [10], the cavity-dependent laser dynamics has been studied in a Kerr-lens mode locked

(KLM) Ti-sapphire laser. When the optical Kerr effect was considered as the nonlinear dynamical parameter, optical bistability and multiple-period bifurcation were numerically demonstrated.

1.3 Laser patterns in degenerate cavity

Even now except for a few special situations, rigorous mathematical existence and completeness proofs for optical resonator eigenmodes do not exist. Because the conventionally laser cavity is an open-side optical resonator, the laser is not a lossless system. Real lasers have never had any difficulty in finding eigenmodes. Empirical and experimental evidence show the same results of lossless system, such as microwave cavities or microwave waveguide, the eigenmodes of laser resonator exist. Therefore, the concept of eigenmodes, such as the Laguerre-Gaussian or the Hermite-Gaussian mode, has long time been accepted and provides a physically realistic and meaningful basis for describing laser resonator in real system.

In ray analysis of the resonators, however, a paraxial resonance equation [11] yields the mirror separations of a two-mirror cavity in which any arbitrary rays repeat themselves after an integer number (say N) of return transits. It has been argued that a set of paraxial closed ray paths that is complete in N round trips might also be regarded as a mode of the resonator. By investigating the effects of off-axis pump on the laser with these degenerate resonator configurations [12], it can be found that a symmetric pattern forms for even N and an asymmetric pattern forms for odd N. These results may be accounted for simply by the introduction of multipass

transverse (MPT) modes that self-reproduce after several round trips in terms of the ray matrix analysis but not by the superposition of standard cavity modes.

In the recently study of multi-beam waist mode [13], we can use propagation of Gaussian q-parameter at 1/3-degenerate cavity to realize multipass transverse mode as showed in Fig. 1-2. In accordance with Fig. 1-2(a), in Fig. 1-2(b) we depict the Gaussian-beam evolution in which the first round-trip wave begins with E_{g1} (w_1=aa'/2, $R_1=\infty$) and reproduces itself after three round trips in the cold cavity. Note that a positive *R* represents a divergent wave riding in the propagation direction. The second round trip begins when E_{g2}(w_2=cc'/2, R_2) converges at dd' owing to negative *R*2; which means that the light wave emanates from E_{g2} just as from dd'. The third round trip, with Eg_3($w_3=w_2$, $R_3=-R_2$), is divergent from cc'; however, it seems to emanate from dIdI'. As discussed above, it implies that the locations of aa', dd', and dIdI' are point sources, respectively, therefore it can be expected that three beam waist can be observed after focusing this laser mode.

If we place a transform lens with a focal length of 5.2 cm a distance of 10.5 cm from a plano-concave cavity which operated at 1/3-degenerate cavity with cavity length of 6cm, this is equivalent to propagating a distance of 16.5 cm from the flat mirror and then through the transform lens. Therefore, three point sources at dd', aa', and dIdI', in the Fig. 1-2 (b), have distances of 10.5cm, 16.5cm, and 22.5cm from the transform lens respectively. An image formula of Gauss is used to determine the locations of images, as a result, three images are located at 10cm, 7.8cm, and 6.8cm,

respectively. A charge-coupled device (CCD) directly images the mode pattern behind the transform lens and in order to reduce the noise, a laser line filter was placed in front of the camera lens of CCD. The images according with distance are shown in Fig. 1-3. It is clearly that the experiment results fit with the calculation of geometric optics and the model of multipass transverse mode.

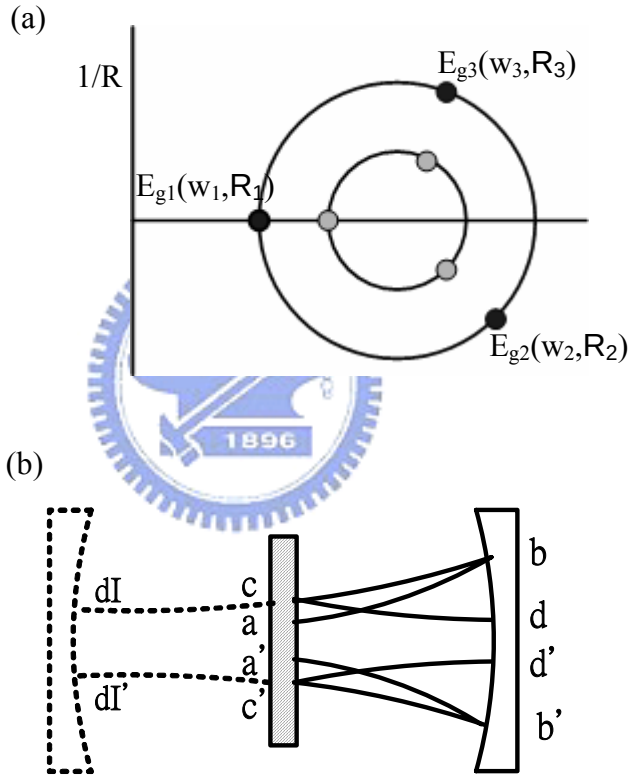

Fig. 1-2 The sketch of multipass transverse mode at 1/3-degenerate cavity. (a) Periodic orbits of the q-parameter for the empty cavity. The two concentric circles mean that there are infinite sets of period-N solutions. (c) Gaussianbeam evolution in the empty cavity.

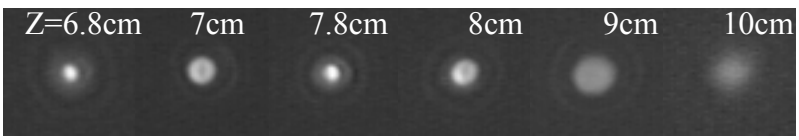

Fig. 1-3 Propagation of the multi-beam waist mode.

In fact, the multi-beam waist made can be explained as a supermode [14-15]. The supermode is superposed by many high-order degenerate transverse modes, and because of cooperative frequency locking of the degenerate modes the laser pattern is temporal stationary. In addition, the pattern propagating in free space along the beam axis is not stationary due to the interference of the degenerate modes. The concept of eigenmodes also can well explain the experiment results, although it needs a serial of calculation but not an intuitional process. Nevertheless, it is interesting that a complicated problem of wave optics can be simplified to a geometrical optics one.

1.4 Aims of this research

In this research, we will investigate the laser dynamics under stationary laser parameters in a simple plano-concave tightly-focused end-pumped Nd:YVO_4 laser near the degenerate resonators, and a model of Huygens's integral together with the rate equations will help us to analyze this laser system.

We found that the laser instability occurs in a very narrow range of cavity tuning on each side of the degeneracy points that shows periodic, period-doubling, and chaotic time evolutions. In our experiment, an extremely small w_p will increase the mode weights of the high-order degenerate modes to as much as the fundamental Gaussian mode. Although so many degenerate modes which bring a supermode join to laser instabilities, the dynamic behaviors on short-cavity side are only temporal instabilities, the instabilities on the long-cavity side are spatiotemporal which results from the

nonlinear coupling between the supermode and the other Laguerre-Gaussian modes. From the simulation model, we found that the other Laguerre-Gaussian modes are introduced by the thermal lens effect. It is the first time to discuss the relationship between the laser instability and thermal lens effect.

Under tightly-focused pumping, the supermode is formed around the degenerate cavity. We utilize the supermode to directly generate various optical bottle beams at different degenerate cavities. An optical bottle beam has a low-intensity zone surrounded by a high intensity shell that can be applied to trap low-index micro-particles or blue-detuned atoms. Optical bottle beams had been generated in the use of holograph, spatial light modulator, and two-beam interference. Those methods need enormous calculation to prepare a suitable holograph with low conversion efficiency or well control of phase retardation for each pixel of SLM and two overlapped beams to make the destruction interference occurring at the beam center. Our method of generating bottle beams directly from a simple laser is convenient for various applications.

We will also investigate the spectrum of laser at degenerate cavities. In a standing wave resonator, the spatial hole-burning effect can be suppressed. This laser can attain very high intensity in the gain medium due to shrinkage of its beam waist to match the pump beam and therefore most of its gain is depleted even by the standing wave. This experimental result proves a useful method to control the mode selection in this degenerate cavity, instead of using otherwise additional dispersion components such as filters or gratings.

In this dissertation, it will introduce the simulation model which includes how the thermal lens effect substitutes or modifies the model in Chapter 2. And than we will discuss our experimental results which are laser dynamics in Chapter 3, directly generation of optical bottle beam in Chapter 4, and optical spectrum of around degenerate cavity in Chapter 5. Finally, in Chapter 6 it will state the conclusions and then give suggestions for future work.

References

[1]. M.D. Wei and W.F. Hsieh, J. Opt. Soc. Am. B 17, 1335 (2000).

[2]. M.D. Wei, W.F. Hsieh, and C. C. Sung, Opt. Commu. 146, 201 (1998).

[3]. Y.F. Chen and Y.P. Lan, Phys. Rev. A 63, 063807 (2001).

[4]. C.H. Chen, M.D. Wei and W.F. Hsieh, J. Opt. Soc. Am. B 18, 1076 (2001).

[5]. P. Laporta and M. Brussard, IEEE J. Quantum Electron. 27, 2319 (1991).

[6]. H. H. Wu and W. F. Hsieh, J. Opt. Soc. Am. B **18**, 7-12 (2001).

[7]. V. Couderc, O. Guy, A. Barthelemy, C. Froehly, and F. Louradour, Opt. Lett. 19, 1134 (1994).

[8]. L. A. Lugiato, G. L. Oppo, J. R. Tredicce, L. M. Narducci, and M. A. Pernigo, J. Opt. Soc. Am. B 7, 1019 (1990).

[9]. J. R. Tredicce, E. J. Quel, A. M. Ghazzawi, C. Green, M. A. Pernigo, L. M. Narducci, and L. A. Lugiato, Phys. Rev. Lett. 62, 1274 (1989).

[10]. J. H. Lin, M. D. Wei, and W. F. Hsieh, J. Opt. Soc. Am. B 18, 1069 (2001).

[11]. Ramsay and J. J. Degnan, Appl. Opt. **9**, 385 (1970).

[12]. E. Siegman, Laser (Mill Vally, CA, 1986).

[13]. C. H. Chen, P. T. Tai, W. F. Hsieh, and M. D. Wei, J. Opt. Soc. Am. B 20, 1220 (2003).

[14]. C. H. Chen, P. T. Tai, W. H. Chiu, and W. F. Hsieh, Opt. Commu. 245, 301 (2005).

[15]. L. A. Lugiato, G. L. Oppo, M. A. Pernigo, J. R. Tredicce, and L. M. Narducci, Opt. commun. 68, 63 (1988).

Chapter 2 Simulation model for our laser system

Fox and Li approach [1-3] is usually used to elucidate the physical picture of radiation in an optical resonator, which repeatedly circulates around the cavity that contains a thin slab gain medium. The transverse mode profile can be calculated based on the central laser wavelength because the diffraction effect experienced by transverse modes will be essentially the same for those any one of axial mode frequencies within the oscillation bandwidth. In the numerical procedure, an arbitrary initial field will eventually converge to a state which the mode profile will self-consistent after one round-trip. In our study [4], we use this approach to simulate an end-pumped solid-state laser.

2.1 Huygens's integral and ABCD matrix

2.1-1 Huygens's integral

In the classical optics, we can use Huygens's integral to describe an optical field after a certain distance of diffraction. So we also can use Huygens's integral to describe laser beam in a real resonator. In Fig. 2-1, it is a sketch of one-dimension Huygens's integral, and it means that the optical field of plane Z_2 interferes with all of the point sources of plane Z_1. In one-dimension condition, the Huygens's integral is

$$\tilde{u}_2(x_2) = \sqrt{\frac{j}{L\lambda}} \int_{-\infty}^{\infty} \tilde{u}_1(x_1) \exp[-jk\rho(x_1, x_2)] dx_1 \,, \tag{2.1}$$

where the $\tilde{u}_1(x_1)$ and $\tilde{u}_2(x_2)$ are respectively the wave functions of Z_1 and Z_2 plane, k is the wave number and λ is the wavelength of laser field. The $\rho(x_1,x_2)$ is the distance of the arbitrary position vectors on the Z_1 and Z_2 planes. Therefore we can define ρ as

$$\rho(x_1, x_2) = \sqrt{L^2 + (x_2 - x_1)^2} \approx L + \frac{(x_2 - x_1)^2}{2L}, \tag{2.2}$$

We can use Eq. (2.1) and (2.2) to calculate the diffraction of optical field.

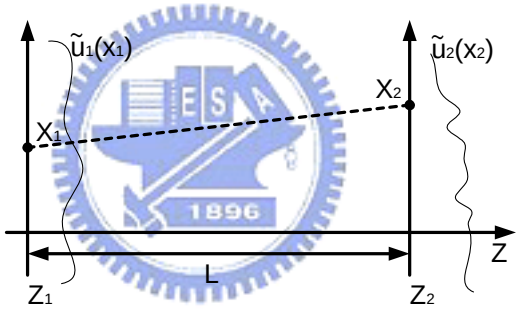

Fig. 2-1 The sketch of one-dimension Huygens's integral. L is the separation distance between plane of Z_1 and Z_2, the $\tilde{u}_1(x_1)$ and $\tilde{u}_2(x_2)$ are the wave function of each plane.

2.1-2 Relationship between ABCD matrix and Huygens's integral

We usually use the ABCD matrix to present a paraxial system, such as laser resonator. If we substitute the elements of ABCD matrix to Huygens's integral, it will be very convenient for using.

Now, we will find the relationship between $\rho(x_1,x_2)$ and ABCD matrix, and substitute to Huygens's integral. In Fig. 2-2, a paraxial optical system between the plane of Z_1 and Z_2 can be expressed as

$$\begin{bmatrix} x_2 \\ x_2^{'} \end{bmatrix} = \begin{bmatrix} A & B \\ C & D \end{bmatrix} \begin{bmatrix} x_1 \\ x_1^{'} \end{bmatrix}, \tag{2.3}$$

where the x and x' respectively represent the positions and slopes of the ray on the Z_1 and Z_2 planes. From the Eq. (2.3), we can get the slope of each point as

$$\begin{aligned} x_1^{'} &= \frac{x_2 - Ax_1}{B} \\ x_2^{'} &= \frac{Dx_2 - x_1}{B} \end{aligned}. \tag{2.4}$$

The input ray may be viewed as a ray coming from an object point P_1 located a distance R_1 behind the input plane, as shown in Fig. 2-2. Hence R_1 and R_2 is given by

$$\begin{aligned} \frac{R_1}{n_1} &\equiv \frac{x_1}{x_1^{'}} = \frac{Bx_1^{'}}{x_2 - Ax_1} \\ \frac{R_2}{n_2} &\equiv \frac{x_2}{x_2^{'}} = \frac{Bx_2^{'}}{Dx_2 - x_1} \end{aligned}. \tag{2.5}$$

Fermat's principle says that "all rays connecting two conjugate points must have the same optical path length between two points." Therefore the ray path from P_1 to P_2 through x_1 and x_2 will equal to the ray path along the optical axis ($\overline{P_1P_2} = \overline{P_1x_1x_2P_2}$). Both ray paths can be written as

$$\begin{aligned} \overline{P_1P_2} &= n_1R_1 + L_0 - n_2R_2 \\ \overline{P_1x_1x_2P_2} &= n_1(R_1^2 + x_1^2)^{1/2} + \rho(x_1, x_2) - n_2(R_2^2 + x_2^2)^{1/2} \\ &\approx n_1(R_1 + \frac{x_1^2}{2R_1}) + \rho(x_1, x_2) - n_2(R_2 + \frac{x_2^2}{2R_2}) \end{aligned}. \tag{2.6}$$

From Eq. (2.6), we can get

$$\rho(x_1, x_2) = L_0 + \frac{1}{2B}(Ax_1^2 - 2x_1x_2 + Dx_2^2). \tag{2.7}$$

By substituting Eq. (2.7) into Eq. (2.1), the Huygens's integral becomes

$$\tilde{u}_2(x_2) = \sqrt{\frac{j}{B\lambda}} \exp[-jkL_0] \int_{-\infty}^{\infty} \tilde{u}_1(x_1) \exp[-j\frac{\pi}{B\lambda}(Ax_1^2 - 2x_1x_2 + Dx_2^2)]dx_1 \,. \tag{2.8}$$

Therefore we have the relationship between elements of ABCD matrix and the Huygens's integral.

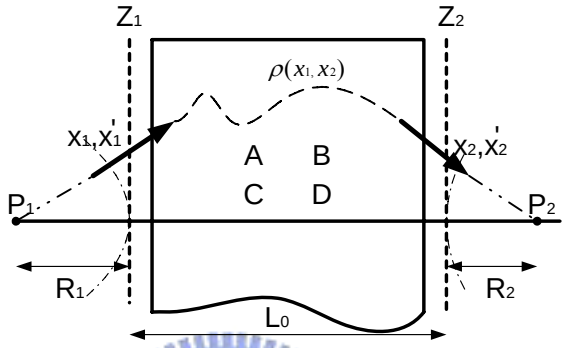

Fig. 2-2 The sketch of the optical ray through an ABCD paraxial system. The x and x' respectively present position and slpoe of ray. P_2 is the conjugate point of P_1.

2.2 Simulation model in a laser cavity

Consider the plano–concave axially pumped solid-state laser shown in Fig. 2-3. It consists of a laser crystal with one of its end faces high-reflection coated as the flat mirror (M_3) and a curved mirror (M_2) with radius of curvature *R* as the output coupler which is separated by a distance *L*. Let the reference plane be the place of M_1 where the light beam just leaves the laser crystal toward the curved mirror. As discussed previously, one can relate the one-dimension Huygens's integral with the ABCD matrix. In this system, we need two-dimension Huygens's integral. However, under cylindrical symmetry, simplified formula can be obtained

$$E_{m+1}^{-}(r) = \frac{j2\pi \exp[\,j2kL]}{B\lambda} \int E_m^{+}(r') \exp\left[\frac{-j\pi}{B\lambda}(Ar'^2 + Dr^2)\right] J_0\left(\frac{2\pi r r'}{B\lambda}\right) r' dr' \,, \tag{2.9}$$

with the round-trip transmission matrix

$$\begin{bmatrix} A & B \\ C & D \end{bmatrix}. \tag{2.10}$$

Here $E_m^{+}(r')$ and $E_{m+1}^{-}(r)$ are the electric fields of the mth and the $(m+1)$st round trips on the planes immediately after and before the gain medium (denoted by the superscripts + and -), where r' and r are the corresponding radial coordinates, λ is the wavelength of laser, and J_0 is the Bessel function of zeroth order. In a thin-slab approximation, we can relate the electric fields E_{m+1}^{+} to E_{m+1}^{-} (after and before the gain medium) in the same round trip as

$$E_{m+1}^{+}(r) = E_{m+1}^{-}(r) \exp[\sigma \Delta N_{m+1} l] \times \rho \times \Pi(r/a)\,, \tag{2.11}$$

where $1 - \rho^2$ is the round-trip energy loss, σ is the stimulated-emission cross section, ΔN is the population inversion per unit volume, d is the length of the active medium, and $\Pi(r/a)$ is an aperture function that Eq. (2.9) is valid for r less than aperture radius a and equals 0 otherwise. Furthermore, assuming that the evolution of the population inversion follows the rate equation of a four-level system, we can write the rate equation as

$$\Delta N_{m+1} = \Delta N_m + R_{pm}(N_0 - \Delta N_m)\Delta t - \gamma_a \Delta N_m \Delta t - (E_m^2 / E_s^2)\Delta N_m \Delta t \,, \tag{2.12}$$

where R_{pm} is the pumping rate, Δt is the travel time through the gain medium, E_s is the saturation parameter, γ is the spontaneous decay rate, and N_0 is the total density of the active medium. This method was used to model a

single-longitudinal multi-transversal high-power solid-state ring laser [5-7] and to analyze the decay rate of standing-wave laser cavity in the linear regime [8]. It was found that a standing-wave resonator can be approximated by a ring resonator if a thin gain medium is placed close to one of the end mirrors [9]. For a continuous Gaussian pump profile $R_{pm} = \mathrm{R}_{\mathrm{p0}} \exp[-r^2 / 2w_p^2]$ with constant pumping beam radius w_p throughout the active medium (thin slab), the total pumping rate over the entire active medium is

$$\int R_{pm} dV = \frac{P_p}{h\upsilon_p}, \tag{2.13}$$

where P_p is the effective pumping power and $h\nu_p$ is the photon energy of the pumping laser. Because we consider only single-longitudinal-mode dynamics, we have omitted the dispersion of the active medium and the gain is assumed to be real. Therefore we have four control parameters: ρ, R, w_p, and P_p, which play important roles in the laser system and will be investigated in detail.

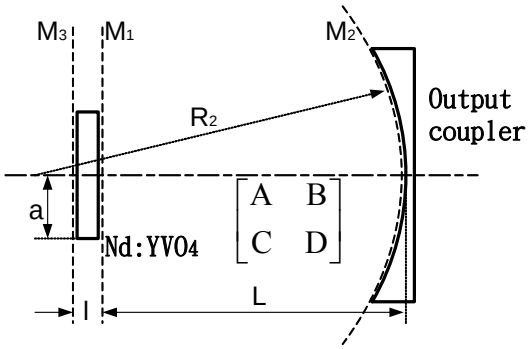

Fig. 2-3 The sketch of plano-concave cavity.

2.3 Thermal lens and modification of simulation model

In continuous-wave (CW) end-pumped solid-state lasers, one must consider thermal effects that will impact optical performance. One important effect, thermal lens, results from temperature-induced changes in the refractive index of gain medium [10].

The periphery of the laser crystal is held at constant temperature by a heat sink. Fig. 2-4 shows the side view and end view of laser rod and heat sink. In the steady state

$$\nabla \cdot h(r,z) = Q(r,z), \tag{2.14}$$

where h is the heat flux, and Q(r,z)=dP(r,z)/dV is the power per unit volume deposited as heat in the laser crystal. The heat flux is related to the corresponding temperature distribution within the crystal by

$$h(r,z) = -K_c \nabla T(r,z), \tag{2.15}$$

where K_c is thermal conductivity of laser material. From Eq. (2.14), we can integrate over a crystal volume bounded by a Gaussian surface of radius r and infinitesimal thickness Δz. This yields

$$2\pi \Delta z h = \int_{z}^{z+\Delta z} \int_{0}^{r} \frac{dp(r',z')}{dV} 2\pi r' dr' dz'. \tag{2.16}$$

Now

$$dP(r,z)/dV = \alpha I_h(r,z), \tag{2.17}$$

where α is the absorption coefficient of gain medium and $I_h(r,z)$ is the intensity of incident pump light that results in heating of the crystal. It is assumed that

$$I_h(r,z) = I_{oh} \exp\left(-2r^2/W_p^2\right) \exp(-\alpha z). \tag{2.18}$$

In Eq. (2.18), I_{oh} is the incident heat irradiance on axis and w_p is the pumping spot. Substituting Eqs. (2.17) and (2.18) into (2.16) and performing the integration yields

$$h(r,z)=\frac{\alpha P_{ph}}{2\pi}\exp(-\alpha z)\left[\frac{1-\exp\left(-2r^2/w_p^2\right)}{r}\right], \tag{2.19}$$

where $P_{ph}=\pi w_p^2 I_{oh}/2$ is the fraction of pump power that results in heating. Substituting Eq. (2.19) into (2.15) and integrating to the crystal boundary, r_b, the steady-state temperature is

$$\Delta T(r,z)=\frac{\alpha P_{ph}\exp(-\alpha z)}{4\pi K_c}\left[\ln\left(\frac{r_b^2}{r^2}\right)+E_1\left(\frac{2r_b^2}{w_p^2}\right)-E_1\left(\frac{2r^2}{w_p^2}\right)\right], \tag{2.20}$$

where $\Delta T(r,z)=T(r,z)-T(r_b,z)$ and E_1 is the exponential integral function [11]. Therefore the total phase change $\Delta\phi$, that is accumulated in a single pass by the pumping through the laser rod, is given by

$$\Delta\phi(r)=\int_0^l K\Delta n(r,z)dz, \tag{2.21}$$

where $\Delta n(r,z)=\Delta T(r,z)\times dn/dT$.

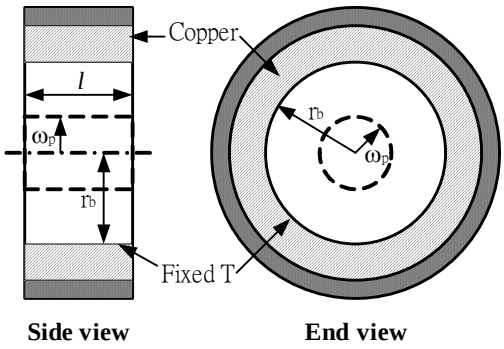

Fig. 2-4 Side view and end view of an applicable laser rod and heat sink. The length of rod is l, the rod radius is r_b, and the $1/e^2$ radius of the Gaussian pump spot is ω_p.

In order to easily estimate the thermal lens, in the previously study [10], they used quadratic power of r to approximate the solution of Eq. (2.21). Because the tightly-focused pumping beam is used in our experiment, the approximate solution is inappropriate to express the phase change resulting from the thermal lens effect. Therefore the numerical solution of Eq. (2.21) is necessary for substituting into Eq. (2.11) to simulate our laser system.

2.4 Conclusion

As discussed above, the simulation model contains a Huygens's integral and a rate equation. In an end-pumped solid-state laser, thermal induced change of refractive index will deform the phase of electric field. We can introduce the radial phase distribution which results from thermal lens to the simulated laser system.

To obtain the time evolution of the output power, we set the reference plane with a 600 μm aperture at the flat end mirror and laterally integrated the intensity profile for each round trip. The parameters that were used are the stimulated emission cross section of 25×10^{-19} cm^2, the spontaneous decay rate of 2×10^4 s^{-1}, the saturation parameter of the active medium of 1.12×10^{10} $J\ F^{-1}\ m^{-2}$, the fractional thermal loading of 0.23, the absorption coefficient of the laser crystal of 1930 m^{-1}, the thermal conductivity of $5.23 Wm^{-1}\ K^{-1}$, the thermal-optic coefficient of 8.5×10^{-6} K^{-1}, and the others are the same as described in Section 3.2.

We use a model of the Huygens's integral together with the rate equations to simulate a real laser system. Because the thermal lens effect is very important in an end-pumped laser, we add numerical model of thermal

induced additional phase to modify our simulation. However, if it is necessary in the numerical, we can add or remove thermal lens effect to observe the influence of thermal. This is a useful numerical model which will be used in the following chapters to analyze our experiment results.

References

[1]. G. Fox and T. Li, Bell Sys. Tech. J. 40, 453 (1961).

[2]. G. Fox and T. Li, IEEE J. Quantum Electron 2, 774 (1966).

[3]. G. Fox and T. Li, IEEE J. Quantum Electron 4, 460 (1968).

[4]. H. Chen, M. D. Wei, and W. F. Hsieh, J. Opt. Soc. Am. B 18, 1076 (2001).

[5]. F. Hollinger and Chr. Jung, J. Opt. Soc. Am. B **2**, 218 (1985).

[6]. R. Hauck, F. Hollinger, and H. Weber, Opt. Commun. **47**, 141 (1983).

[7]. F. Hollinger, Chr. Jung, and H. Weber, Opt. Commun. **75**, 84 (1990).

[8]. Y. J. Cheng, P. L. Mussche, and A. E. Siegman, IEEE J. Quantum Electron. **31**, 391 (1995)

[9]. M. Moller, L. M. Hoffer, G. L. Lippi, T. Ackemann, A. Gahl, and W. Lange, J. Mod. Opt. **45**, 1913 (1998).

[10]. M. E. innocenzi, H. T. Yura, C. L. Fincher, and R. A. Fields, Appl. Phys. Lett. 56, 1831 (1990).

[11]. M. Abramawitz and I. A. Stegun, Handbook of mathematical functions (Dover, New York, 1965)

Chapter 3 Laser dynamics around 1/3-degenerate cavity

In this chapter, we will control cavity length, pump power and pump spot to study the cavity-configuration dependence of laser instability and to determine the regions of laser instability. When the pump size is small, we found that the laser always exhibits a stable cw output, except for a narrow range of cavity tuning on each side of the degeneracy. The laser output shows self-pulsation with periodic, period-doubling, and chaotic evolutions. We also observed various patterns of the far field when we scanned the cavity length. In particular, an anomalous mode pattern is accompanied with frequency beating close to the point of degeneration. The simulation in use of Huygens's integral and rate equations, while taking into account the thermal lens effect, shows good agreement with the experiment.

3.1 Introduction

It is commonly believed that spontaneous instabilities are impossible in class B lasers described by simple two-level rate equations without an additional degree of freedom such as external modulation, light injection, or delayed feedback, etc. [1]. However, the transverse effects such as gain variation and diffraction in the resonator provide the additional degrees of freedom and have been demonstrated to play important roles in lasers [2, 3]. Because various transverse modes may be excited especially when the laser

is operated at near-degeneracy, a degenerate resonator is thus a good choice for obtaining laser instabilities. Previously, we have analyzed an iterative map of the q-parameter of the resonator [4] and concluded that a laser will become unstable near some degenerate cavity configurations under nonlinear effects. Using an end-pumped cw Nd:YVO4 laser, we have studied different laser behaviors under various pump sizes [5,6] when the cavity is near 1/3-transverse degeneracy (g_1g_2=1/4). Recently, the Petermann K factor has also been calculated for maxima on each side of the degeneracy under strong gain guiding or small pump size [7]. It was emphasized that in the vicinity of the degeneracies the empty-cavity degenerate transverse modes are phase-locked and the resultant radial phase profile depends strongly on the cavity-length detuning.

3.2 Experiment setup

The experimental setup is schematically shown in Fig. 3-1. This laser contains a 1-mm thick Nd:YVO4 laser crystal whose one end face acted as an end mirror and a spherical mirror with radius of curvature of 8 cm as the output coupler (OC). A cw near-TEM_{00} Ti–sapphire laser at wavelength of 808 nm was used as the pump source, which was focused by a collimating lens onto the crystal so the pump size was adjustable. The end face of the crystal, which acted as the end mirror and faced to the pump beam, had a greater than 99.8% reflectivity at 1.064 μm and greater than 99.5% transmission at 808 nm; the other end face comprised an antireflection layer at 1.064 μm to avoid the effect of intracavity etalons. The OC of 10% transmission was mounted upon a translation stage so we could tune the

cavity length (L) near the degenerate configuration. The degeneration point of g_1g_2=1/4, which corresponds to L=6 cm, was determined by the cavity length where the lowest lasing threshold occurs [8]. The laser output was split into two beams, one of which was recorded by a CCD camera and the other was further split into two beams that were individually collected by two photodiodes (PDs) with rise times<0.3 ns. The signals of the PDs were then fed into a LECROY-9450A oscilloscope (bandwidth 200 MHz) and an HP8560E RF spectrum analyzer (bandwidth 2.9 GHz), respectively. The Gaussian pump radius, w_p, was determined by the standard knife method.

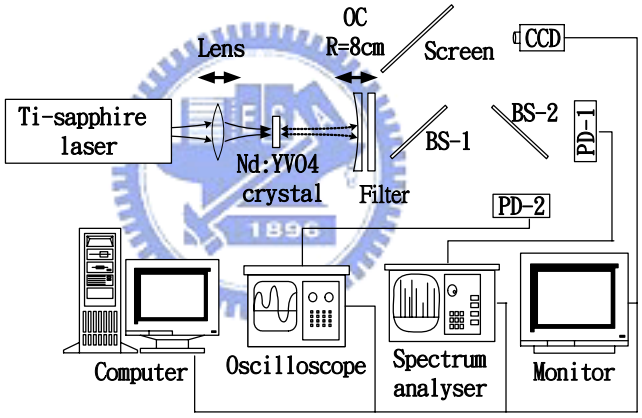

Fig. 3-1 The schematic experimental set up. BS is the beam splitter.

3.3 Experimental results and discussions

3.3-1 Locations of spontaneous instability

The output power varied with the cavity length under various pump radii and is shown in Fig. 3-2(a). The bottom three curves for w_p=19 μm show that a higher pump power not only widens but also heightens the power hump. The laser exhibits a stable cw output for almost entire range of the

studied 3-mm cavity tuning. However, within a narrow range of L on each side of the power hump, denoted as stars in Fig. 3-2(a), we always observed spontaneous instabilities. The top two curves are the cavity-dependent output power for w_p=25 and 34 μm at a pump power of 300 mW, in which the triangles and the solid circles denote the unstable regions for both cases. Note that the radius of cold-cavity fundamental mode is approximately 108 μm. Summarized in Fig. 3-2(b) are the unstable regions in terms of the cavity length and the pump power for the three pump sizes of 19, 25, and 34 μm. We use a single symbol to denote a narrow unstable region while twin symbols are used to encompass a wider unstable region of about 100 μm. One can see that the unstable regions on the short-cavity side are well separated for different w_p and located farther away from degeneracy with increasing the pump power; in contrast, those on the long-cavity side are located very close to the point of degeneration and are nearly independent of the pump power.

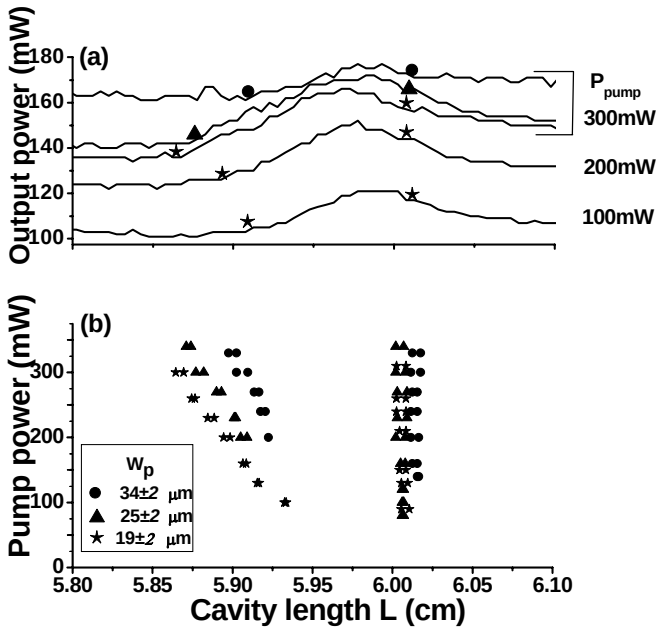

Fig. 3-2 The observed output power as a function of cavity length (a) and the unstable regions in terms of the cavity length and the pump power for different w_p (b). The symbols for w_p are the same in (a) and (b). The output power is around 40 mW for P_{pump}=100 mW as w_p=19 μm. Note that we have added 50 mW and 75 mW for the curves of P_{pump}=200 mW and P_{pump}=100 mW. The absorption efficiency of P_{pump} is about 60-70%. The lasing threshold is about 5-30 mW depending on L and w_p.

We use our simulation model which was discussed in chapter 2 to simulate the output power with the cavity length and find out the location of instability. Fig. 3-3(a) shows the output power as a function of L!when considering the thermal lens effect. The curves of output power that are labeled as triangles, empty squares, and solid circles for w_p=25, 30, and 35 μm, respectively, show asymmetric power humps with respect to the point of degeneration. The dependence of the power hump on w_p and P_p (the effective pump power) are the same as in Fig. 3-2(a). The unstable regions are summarized for four values of w_p in Fig. 3-3(b), which are similar to those in Fig. 3-2(b) except that the vertical axis of Fig. 3-3 is the effective

pump power that matches with the pump efficiency of ~0.6 taken from the measured pumping. Again, in Fig. 3-3(b) we use a single symbol to denote a narrow unstable region while twin symbols are used to encompass a wider unstable region. It shows similar unstable regions and dependence on w_p and P_p as those in Fig. 3-2(b); for example, at w_p=35 μm, the unstable region shifts approximately from L=5.94 to 5.90 cm on the short-cavity side as one increases the effective pump power to match with the experimental data in Fig. 3-2(b). Moreover, the far-field intensity profiles beside the long-cavity unstable region are similar to those in Fig. 2(b) of [6]. In addition, no instability can be observed as w_p>40 μm, which is also consistent with the experiment.

In order to study the influence of the thermal lens effect, we repeated the simulation without considering the thermal lens effect. The calculated output power and the obtained unstable regions are shown in Fig. 3-4(a) and (b), respectively. As compared with Fig. 3-3, it clearly shows that thermal lens effect leads to certain phenomena: (1) an asymmetrical shape of the power hump; (2) asymmetrical unstable regions with respect to the degeneration point; (3) dependence of the region shift on P_p on the short-cavity side but not on the long-cavity side; and (4) much less shift of the power maximum than shift of the unstable region (e.g., see w_p=30 μm and P_p=150 mW).

In summary, adding thermal lens effect in simulation model will obtain similar results with the features of instability regions and the diagram of output power versus cavity length in experiment. No matter how the results of experiment or simulation (with thermal lens or without thermal lens effect)

the instability regions are located at the rim of power hump. If the w_p<40 μm, we can easily locate the instability regions by the diagram of output power versus cavity length.

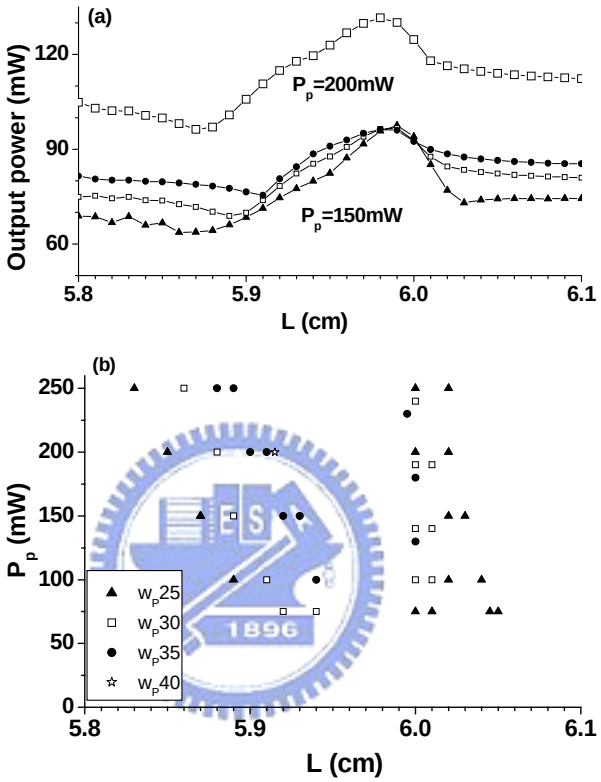

Fig. 3-3 The numerical output power as a function of cavity length with considering the thermal lens effect (a) and the unstable regions (b) for different w_p. The symbols for w_p are the same for (a) and (b).

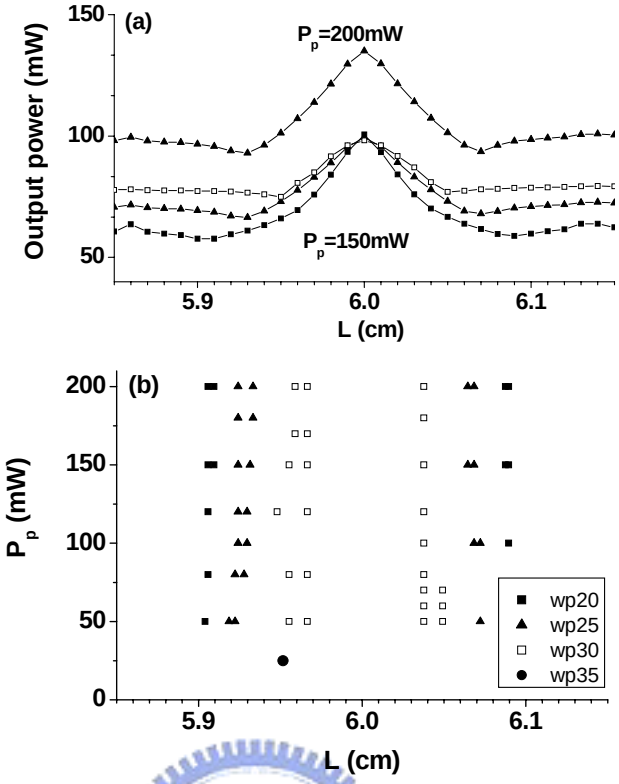

Fig. 3-4 The numerical output power as a function of cavity length (a) and the unstable regions (b) without considering the thermal lens effect. The symbols for w_p are the same for (a) and (b).

3.3-2 Laser dynamics in instability region

When the cavity length was tuned from the long-cavity side toward and across the point of degeneration, various far-field mode patterns were observed. The mode pattern shows a near-fundamental Gaussian distribution far from degeneracy. Tuning L close to the right edge of the unstable region, we observed a slightly distorted mode pattern. When the cavity was set within about 100 μm of the unstable region, the mode pattern became non-cylindrically symmetric and strongly spread in a special direction as shown in Fig. 3-5(a). This anomalous spreading pattern maintained wider than the whole unstable region by few tens of micrometers. When L was tuned across the range that showed the spreading pattern, the

far-field pattern recovered to a cylindrically symmetric one but turned into many concentric rings with a dark center that is the far-field pattern of the multi-beam-waist mode [6]. By further tuning of L!toward the unstable region on the short cavity side, we observed the cylindrically symmetric mode pattern as shown in Fig. 3-5(b) that differs from the patterns in the unstable region of the long-cavity side, as indicated in Fig. 3-5(a).

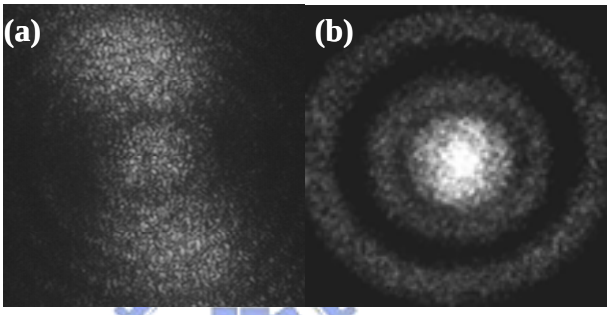

Fig. 3-5 The far-field mode patterns inside the long-cavity unstable region (a) and inside the short-cavity unstable region (b).

We further investigated the temporal behaviors of the output power within the unstable regions at P_{pump}=260 mW and w_p=34 μm. Fig. 3-6(a) shows a periodic time trace when the cavity was tuned at the edge of the long-cavity unstable region. Its corresponding RF spectrum in Fig. 3-6(b) shows one main peak at 1.33 MHz and three harmonics. When the cavity length was decreased by 20 μm from the position of Fig. 3-6(a), a period-2 evolution was observed. The time trace and its spectrum are shown in Fig. 3-6(c) and (d), respectively. On continuing the decreasing of the cavity length, we recorded a chaotic evolution in Fig. 3-6(e) with a broad low frequency spectrum indicated in Fig. 3-6(f). Calculation by use of the chaos data analyzer (American Institute of Physics) shows that the correlation

dimension of the chaotic evolution is approximately 2.1. Although the temporal behaviors of the cavity configuration-dependent instabilities are similar on each side of the degeneracy, the high-frequency responses of their power spectra are quite different. For the long-cavity instabilities we observed multiple beating frequencies at 812 MHz, 1.63 GHz, and 2.44 GHz (see Fig. 3-6(g)) that were confirmed with a Fabry-Perot interferometer (FPI) having FSR=15 GHz and finesse=150. The transverse mode beating pertaining to the Laguerre-Gaussian $LG_{1,0}$ and/or $LG_{2,0}$ modes would induce spatiotemporal instability, where the subscripts 1 and 2 are the radial indices and 0 is the azimuthal index. However, within the short-cavity unstable region the spectrum shows only the longitudinal mode beating at 2.44 GHz with the absence of transverse mode beating in both of the RF and the FPI spectra.

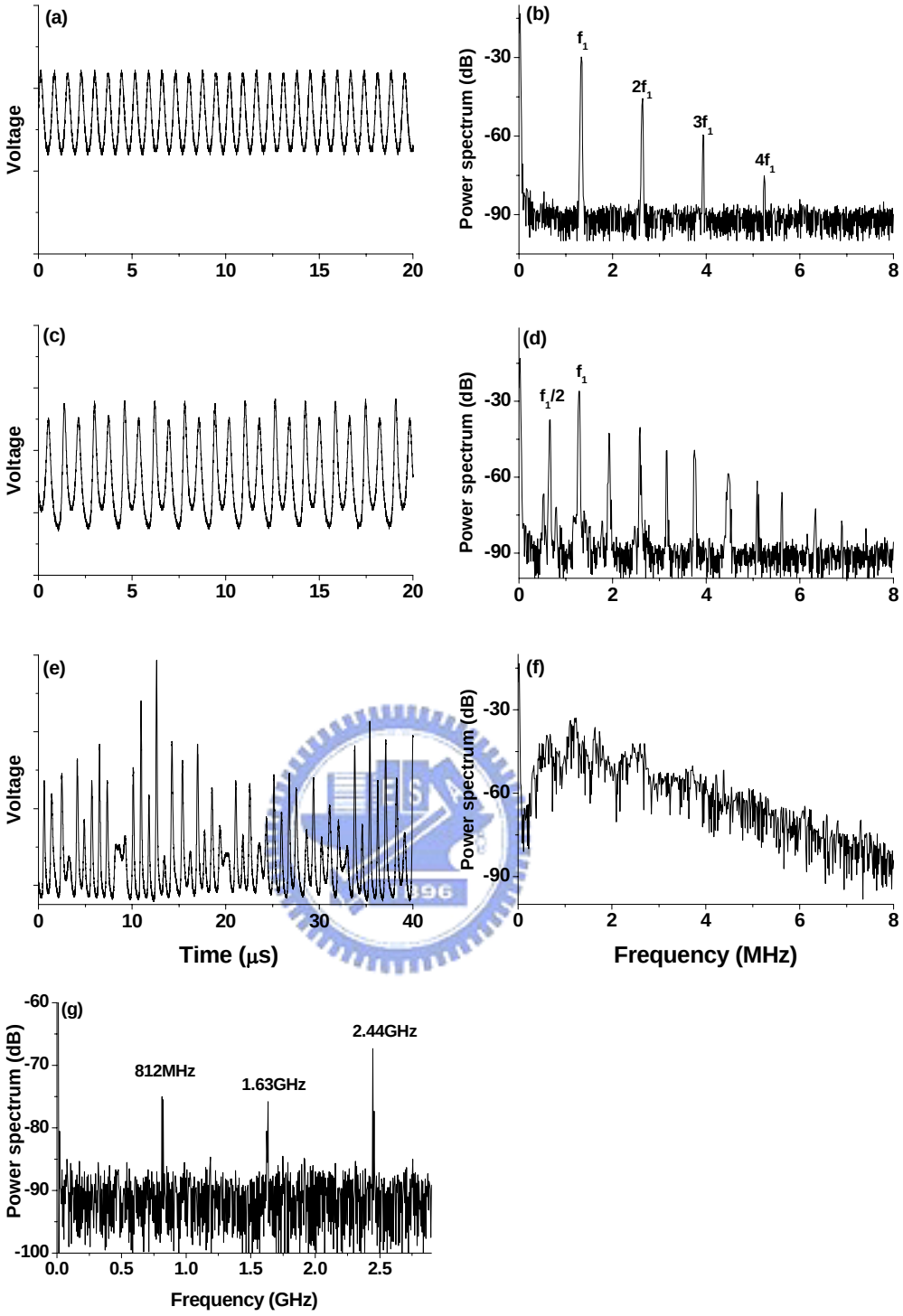

Fig. 3-6 The temporal evolution of laser output. (a) Periodic, (c) period-doubling, and (e) chaotic output within the long-cavity unstable region. The RF spectra (b), (d), and (f), that correspond to (a), (c), and (e), respectively. (g) The high frequency RF spectrum of the spreading mode pattern of Fig. 3-3(a).

To investigate the distinction between the instabilities on the long-cavity

side and those of the short-cavity side, we used two PDs at different transverse positions to simultaneously record the laser power. The first PD was fixed at the center of the profile as the reference and the second one was located at an off-axis position. When the two detectors were separated within a distance, their temporal traces on the oscilloscope were completely the same as shown in Fig. 3-7(a). However, we found for the long-cavity instability that the high peak of one trace coincided with the low peak of the other trace as shown in Fig. 3-7(b) when the two detectors were separated by some specific distance. This reveals that the intensity profile varies with time and thus indicates spatiotemporal instability. On the other hand, within the unstable region of the short-cavity, we always observed the same behavior between the two signals no matter at what position the second PD was located. Temporal instability was exhibited on the short-cavity side. In addition, we also found that the instabilities on both sides of the degeneracy are closely related to high-order transverse modes because the instabilities disappeared when a knife-edge was inserted 500 μm into the cavity beam to inhibit the high-order transverse modes. This will be explained in the following paragraph.

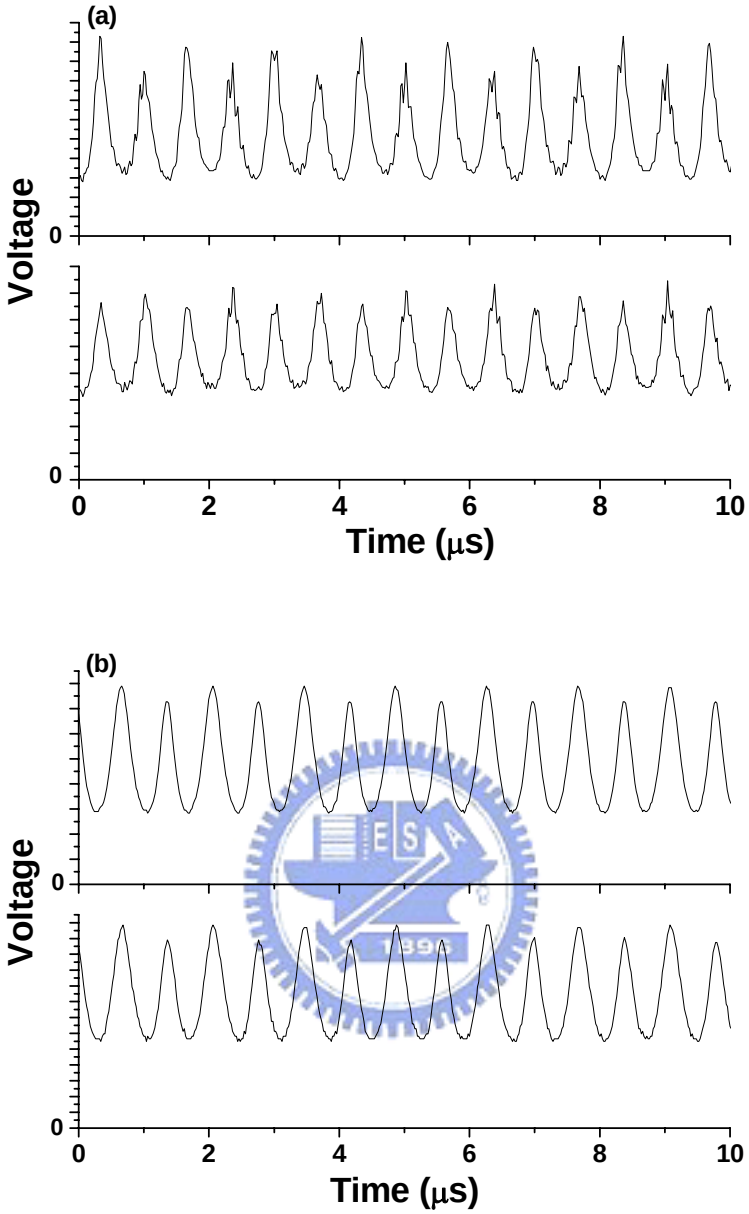

Fig. 3-7 The time traces in oscilloscope when the two PDs were separated close to each other (a) and farther away (b) for the long-cavity instabilities.

We will use our simulation model to explain the observations of experiment. To simplify our discussion, we remove the thermal effect in the simulation. Without the thermal lens effect, not only the power hump but also the dynamical behaviors are symmetric with respect to the point of

degeneration. The simulated temporal evolution of the unstable output power exhibits self-pulsation on both sides of the degeneracy with a pulsing frequency of few hundred kHz (see Fig. 3-8(a)). The simulated intensity profile of each round trip show the variation of the on-axis peak intensity with time as the characteristic feature of Fig. 3-8(a), but the normalized profile varies only a little. We plotted four normalized intensity profiles in Fig. 3-11(b) from the pulse peak to valley to show the variation. Their corresponding far-field intensity profiles [insets in Fig. 3-8(b)], having two obvious rings, agree with the photograph of Fig. 3-5(b). Moreover, the far-field intensity profile decreases smoothly and then increases when the pulse is growing. This leads to pure temporal instability. The modal analysis shows that the modes in Fig. 3-8(b) can be decomposed into the combination of the near-degenerate $LG_{0,0}$, $LG_{3,0}$, /!/!/, $LG_{18,0}$ modes with mode weights and relative phase shifts because $LG_{21,0}$ undergoes large diffraction losses for a 600 μm aperture at the reference plane. These phase shifts must be included because the phase pattern is important as emphasized in [7]. We give a fitted result in the figure caption of Fig. 3-8(b). When the thermal lens effect is included, the feature of self-pulsation is unchanged for the short-cavity side. This matches with the general expectation that the thermal lens effect will only shift the cavity length.

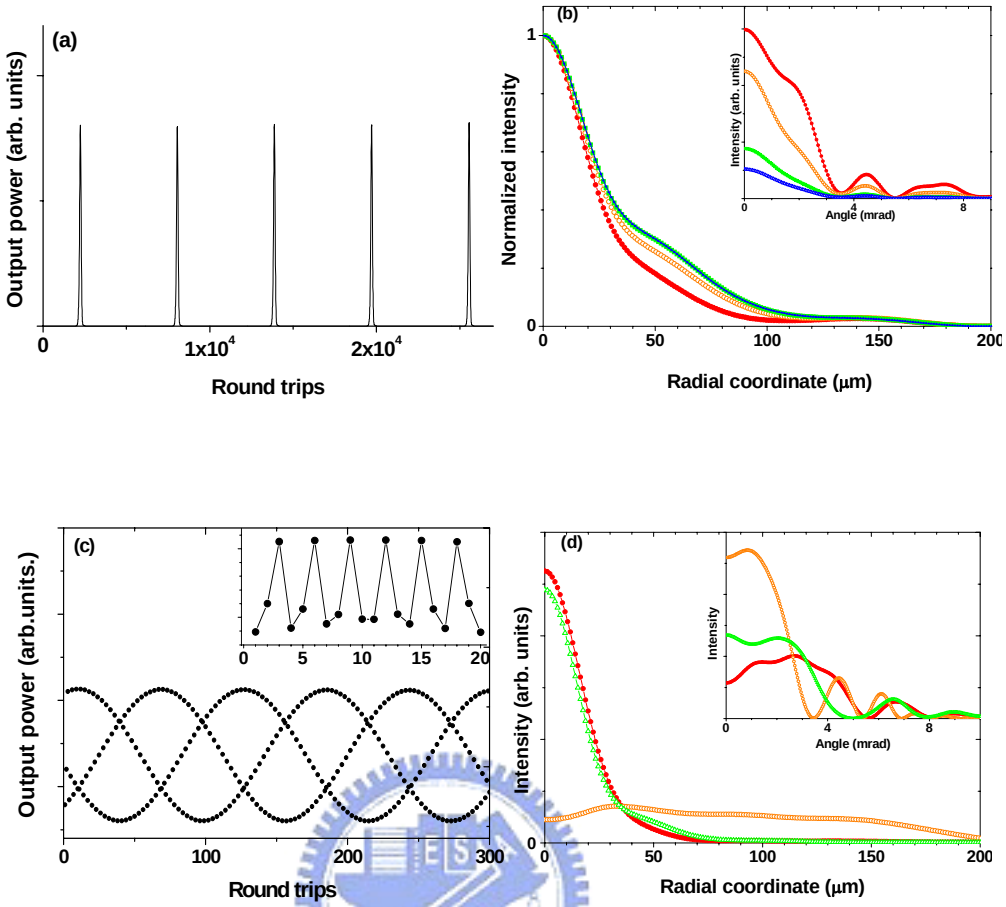

Fig. 3-8 (a) A self-pulsing temporal evolution of the simulated output power without the thermal lens effect for M=5.96 cm. (b) The normalized intensity profiles and their corresponding far-field profiles (inset) from the pulse peak (solid circles) changes to open circles, solid squares and then to the pulse valley (open triangles). The normalized profiles of the open triangles are covered by the solid squares. The modal analysis for the profile of solid squares are $LG_{0,0}(0^\circ)+0.63\ LG_{3,0}(-75^\circ)+0.34\ LG_{6,0}(-105^\circ)+0.16\ LG_{9,0}(-90^\circ)+0.08\ LG_{12,0}(-83^\circ)+0.08\ LG_{15,0}(-116^\circ)+0.07\ LG_{18,0}(-93^\circ)$. (c) The numerical temporal evolution of the output power in the vicinity of the degeneracy with the thermal lens effect for L=6.005 cm. Inset is the first 20 iterations. (d) The intensity profiles and their corresponding far-field profiles (inset) of three successive round trips.

However, on the long-cavity side the region shift seems independent of P_p and the self-pulsation becomes the characteristic feature of Fig. 3-8(c), in which the output power forms three branches of oscillation. The first 20

iterations in the inset show that the output evolution nearly comes back the same value after three round trips; that is the power spectrum indicates one peak at roughly 1/3-longitudinal beating frequency that corresponds to the experimental data of 812 MHz. The intensity profiles of three successive round trips are shown in Fig. 3-8(c), which are not normalized due to the large difference. The corresponding far-field intensity profiles in the inset of Fig. 3-8(d) exhibit a complex feature, which is different from that of the short-cavity side. Unfortunately, we could not yet obtain good fitting data by running the same fitting parameters, even when the $LG_{1,0}$ mode was included. This may be due to the peculiar phase pattern that is deformed strongly by the thermal lens effect in the vicinity of the degeneracy. Because the beating frequency between the near-degenerate LG modes is absent on both long-cavity and short-cavity instabilities, the frequencies of the near-degenerate LG modes are locked together to a single frequency. Therefore the frequency-locked mode, a supermode [9-10], interacts with the inverted populations and thus leads to the short-cavity instabilities. However, the long-cavity instabilities arise mainly from the frequency beating between the supermode and the other empty-cavity modes. Although the asymmetric (spreading) mode pattern of Fig. 3-5(a) cannot be produced by using the cylindrically symmetric model with single optical frequency, the simulated results agree with the experiment of transverse mode beating. As far as we know, this is the first report that discusses the relationship between the instability and the thermal lens effect.

Furthermore, when the aperture on the reference plane is decreased to 450 μm, in accordance with the previous experiment described, the

instability disappears. The stationary mode now consists of the near-degenerate LG modes with the same frequency but lack of the higher-order $LG_{15,0}$ and $LG_{18,0}$ modes. This fact of transverse mode locking was confirmed by the absence of the near-degenerate mode beating and by the observation of the intensity profile variation with the propagation distance as done in [6]. The supermode lack of the components of the $LG_{15,0}$ and $LG_{18,0}$ modes is unable to arise the instability. Inserting a knife-edge into the cavity beam in our experiment also results in a cylindrically symmetric pattern instead of a spreading pattern. Apparently, the high-order modes with small amplitude may play important roles in symmetry breaking as indicated in [11]. However, the origin of the symmetry breaking is still unknown.

Going back to Fig. 3-8(a), the pulsation is damped by the relaxation oscillation so the pulsing frequency depends on the pump power and the cavity length. Theoretically, the pulsing spectrum can be calculated from the Fourier transform of the output power evolution. Interestingly, by using $\gamma=10^5$ s which the spontaneous decay rate is scaled 5 times we obtained periodic pulsing, period-2, and chaotic time evolution of the output power when L!was tuned from 5.96 to 5.951 cm with w_p=30 μm and an effective pump power of 100 mW as show in the Fig. 3-9. After 5 times scaling the dynamic behaviors of simulation, which is the route to chaos, are the same as the observations of experiment.

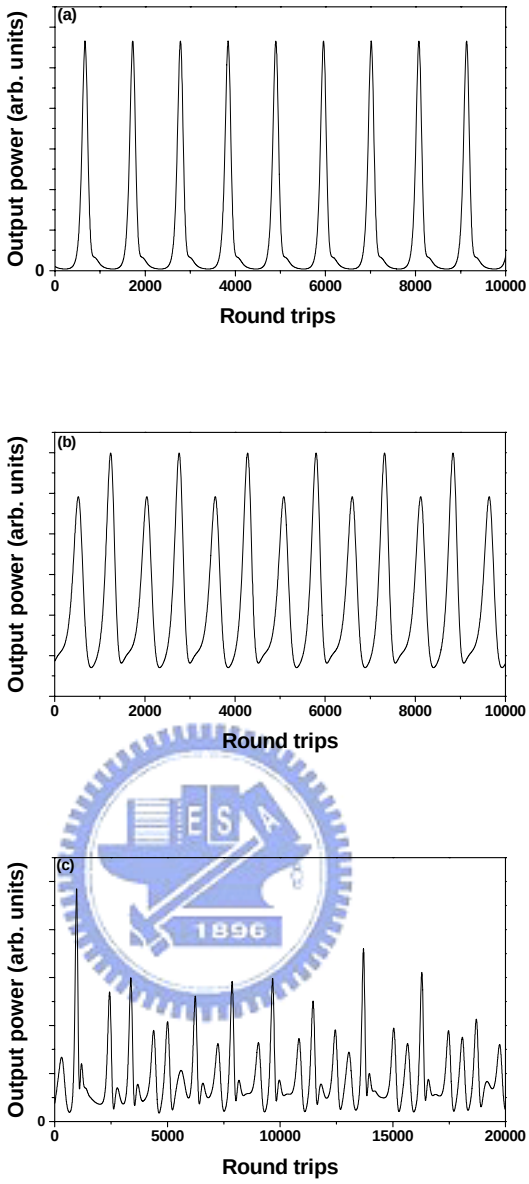

Fig. 3-9 The time evolution of self-pulsation by 10 times scaling. (a) periodic, (b) period-doubling, and (c) chaotic output are respectively located at L=5.955cm, 5.9523, and 5.9505cm.

3.3-3 Cooperative frequency locking and laser patterns

The laser cavity operates at exactly degeneracy, the transverse modes and longitudinal modes will degenerate. It is mean that we can not observe any mode beating on the RF spectrum. When laser resonator away from the degeneracy the mode beating should be measured result in none-degenerate

transverse modes. However, we also can not observe any mode beating in our experiment except the instability of long-cavity as section 3.3-2 discussing above. This phenomenon is called as cooperative frequency locking [12]. In this section we will use mode expansion to discuss laser patterns around degenerate cavity, and we found that vary large range of cooperative frequency locking where about several millimeters. Cooperative frequency locking due to their nonlinear coupling several transverse modes lock to a common optical frequency and particular phase differences are selected [13-14]. In the resulting stationary pattern, amplitudes and relative phases of the interacting modes are determined by the minima of the generalized free energy of the system [15-17]. However, in conventional case, there are only several hundreds micrometer away from degeneracy to maintain frequency locking [18].

3.3-3.1 Mode expansion and experiment observations

We show the normalized intensity profile and the phase profile on the reference plane with solid circles in Figs. 3-10(a) and (b) at the degeneracy (L = 6 cm) for w_p = 30 μm and the effective pump power of 100 mW without considering the thermal lens effect. In order to show the good fitting of mode decomposition using genetic algorithm (GA), we plot the fitted results in Figs. 3-10(a)-(d) with open circles and use the logarithm scale in Fig. 3-10(a). The mode decomposition is done with 13 fitting parameters including six amplitude weightings and seven relative phases. For the aperture radius of 600 μm on the reference plane, we expand the calculated mode profile into the 1/3-degenerate LG_{pm} modes with p = 0, 3, 6,. . . ,18 and

m = 0, where p is the radial mode index and m is the angular index. The normalized electric field of LG_{p0} mode can be expressed as

$$E_{p0}(r,z) = A_{p0}(r,z)\exp\left(\frac{-r^2}{w(z)^2}\right)\exp\left(\frac{ikr^2}{2R(z)}\right)\exp\left\{i\left[kz-(2p+1)\tan^{-1}\left(\frac{z}{z_R}\right)+\delta_p\right]\right\}, \quad (3.1)$$

where

$$A_{p0}(r,z) = E_0\frac{w_c}{w(z)}L_p^0\left(\frac{2r^2}{w(z)^2}\right)$$

is the modal function, E_0 is the normalization constant, z_R is the Rayleigh length, w(z) is the beam radius, R(z) is the radius of curvature of the phase front, r and z are, respectively, the radial and axial coordinates, and L_{0p} is the Laguerre polynomial for mode index p. We assume all the excited LG_{p0} modes have the same wavenumber and then the intensity profile $|\eta_0 E_{00} + \eta_3 E_{30} + \ldots + \eta_{18} E_{18,0}|^2$ with seven amplitude weightings η(η_0 be fixed unity) and seven relative phases δ_p is fitted to the mode-calculation profile. We see that the resultant fitted profiles match with the mode-calculation profiles extremely well in Figs. 3-10(a)-(d). From Fig. 3-10(a) the central lobe of the intensity profile is near-Gaussian with the waist radius of ~30 μm (approximately equals to the pump radius, see the solid curve in the inset with linear scale), which shows that the laser is strongly gain-guided. Note that the radius of the fundamental mode, w_0, is 108 μm. The seriously saturated gain distribution is shown with the dashed curve in the inset of Fig. 3-10(a). The gain distribution is obtained from the term $\exp(\sigma\Delta_0 d)$ in Eq. (2.11), where Δ_0 is r-dependent. Fig. 3-10(b) shows that the phase profile is flat within r = 200 μm but discontinuously jumps π phase at some positions

of r, e.g., the first phase jump at r != 200 μm corresponds to the position of the second intensity zero of the $LG_{3,0}$ mode. The relative phases of the degenerate LG modes for L != 6.0 cm show the degenerate LG modes are not only phase-locked but also nearly in-phase on the reference plane. The unusual result of flat wavefront on the flat end mirror, obtained in our mode calculation including gain, is the same as in [7] and this was discussed therein.

When the cavity length is slightly tuned away from the degeneracy to L != 6.01 cm, the central lobe of the intensity profile shows a slightly distorted Gaussian in the inset of Fig. 3-10(c) with the solid curve in linear scale. Also shown with the dashed curve in the inset is the saturated gain distribution. We can see in Fig. 3-10(d) that the phase pattern is already highly curved for r !< 100 μm and no longer has π-jumps at some positions of r. Note that the phase is continuous at r != 223 μm because the phase jump is 2π. Besides, at L != 6.01 cm the degenerate LG_{p0} modes are no longer in-phase on the reference plane but have monotonically increasing relative phases with the increase of p. Even so, these LG_{p0} modes are still phase-locked to form a stationary mode. Such a stationary mode exhibits profile variation along the propagation distance due to the variation of Gouy phases of the LG_{p0} modes and it is in fact an optical bottle beam that has been presented in [9]. It is worthy to note that nearly the same behavior for the case of L = 5.99 cm except that the phase pattern is inverted within r != 100 μm and the relative phases of the LG_{p0} modes decrease monotonically with increase of p.

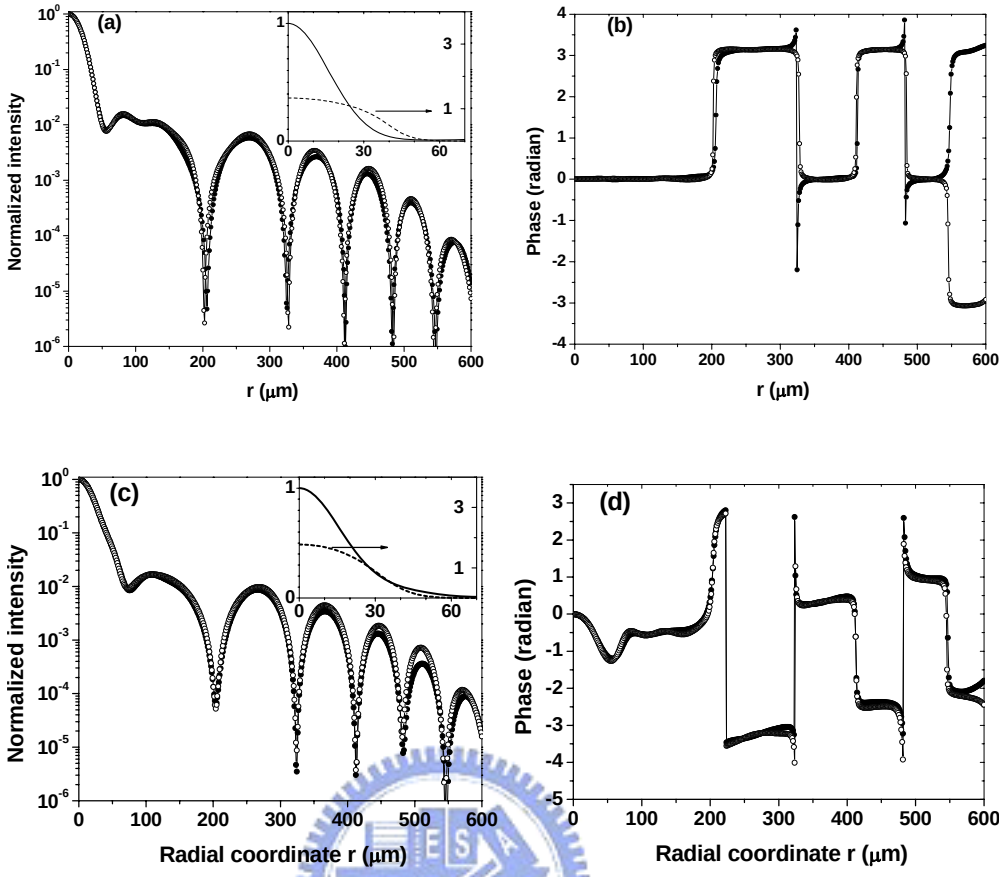

Fig. 3-10 The intensity profile in logarithm scale (a) and the phase profile (b) at the exact degeneracy (L != 6.0 cm) obtained from the mode calculation (solid circles) and from the fitted result of mode decomposition (empty circles). Inset in (a) are the intensity profile in linear scale (solid curve) and the saturated gain distribution (dashed curve). (c) and (d) are, respectively, the intensity and phase profiles for L != 6.01 cm.

At L = 6.05 cm, the intensity profile is much distorted from Gaussian and the phase pattern is highly curved for r < 150 μm. The mode weightings and the relative phases of the LG_{p0} modes for various cavity lengths are summarized in Figs. 3-11(a) and (b) except for the absence of L = 6.04 cm because the laser instability occurs there as section 3.3-1 and -2 discussing above. We can see in Fig. 3-11 that the mode weightings for the case of L = 6.05 cm have significant decrease for p = 3, 6, 9 as compared

with the case of L = 6.03 cm and that the relative phases no longer monotonically increase but alternate for p > 6.

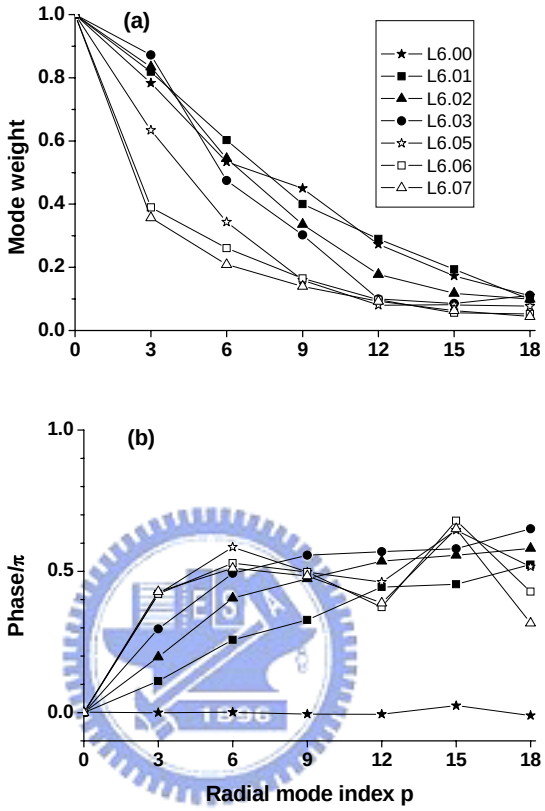

Fig. 3-11 The mode weightings (a) and the relative phases (b) of the LG_{p0} modes as L is tuned away from the degeneracy.

Although the far-field intensity pattern looks like a Gaussian profile when the cavity is tuned far away from the degeneracy to L = 6.10 cm, the mode profile still varies along the propagation. We can see from Fig. 3-12(a) that the calculated mode profile exhibits a dark center from z = 6.8 to 8.0 cm where far from the plane mirror. We therefore used this z-dependent profile to verify the phase-locking of degenerate transverse modes as L is tuned from 5.90 to 6.10 cm. The profile will appear a dark center

approximately from 19 to 23 cm after a convergent lens with focal length of 7 cm when the convergent lens is put behind the output coupler at a distance of 12 cm. Fig. 3-12(b) shows the photograph taken at a distance of 20.5 cm after the convergent lens from our Nd:YVO_4 laser as L is set on the right edge of the phase-locking region. We found experimentally that the phase-locking region has been shifted ~500 μm toward the short cavity side by the thermal lens effect for w_p = 30 μm and pump power of 150 mW.

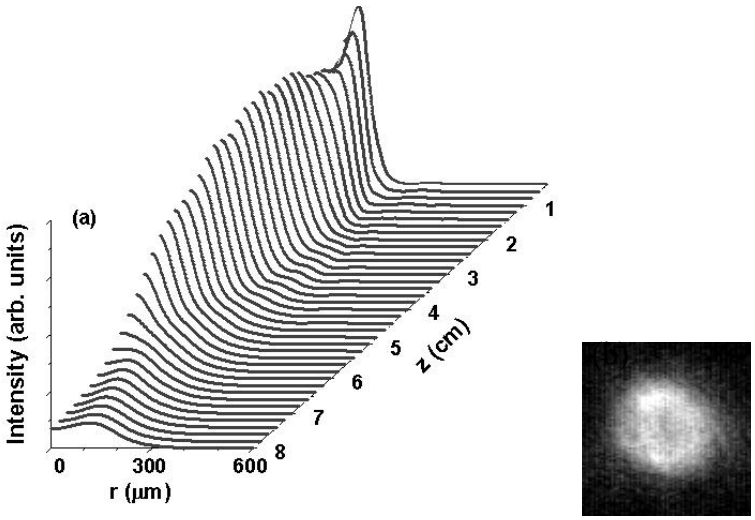

Fig. 3-12 (a) The numerical beam profile variation along the propagation distance z for L = 6.10 cm. The intensity profile with a dark center can be seen at z = 6.8-8.0 cm that is transformed to a distance of 19-23 cm after the convergent lens. (b) The photograph experimentally taken at 20.5 cm after the convergent lens.

3.3-3.2 Briefl summary

We have confirmed the phase-locking of degenerate transverse modes near the degeneracy of $g_1g_2 = 1/4$ in a tightly focused end-pumped Nd:YVO4 laser that can be verified by observation of beam profile variation along the propagation distance within a large cavity-length detuning from the

degeneracy. We also decomposed the stationary lasing mode into the degenerate Laguerre-Gaussian modes with their relative locked phase.

3.4 Conclusion

We have found the cavity-configuration-dependent instabilities and determined the two sets of the unstable regions beside the degeneracy near $g_1g_2=1/4$ in an end-pumped Nd:YVO4 laser with small pump sizes. We illustrated the temporal behavior of the instabilities including the chaotic output. The different far-field patterns beside the unstable regions were observed; in particular, a special spreading mode pattern was observed in the vicinity of the degeneracy. Our numerical results, which were obtained using a cylindrically symmetric model with single frequency, agree well with the experiments and reveal the influence of the thermal lens effect.

Even far about 1mm from degeneracy, we also can observe the phenomenon of cooperative frequency locking in the experiment. In the numerical, we use GA to realize mode weight of each degenerate mode and its corresponding phase. When we operate the laser cavity at exactly degeneracy, all degenerate modes are nearly in-phase on the reference plane. This study will help us to control transverse mode for application.

References

[1]. C.O. Weiss and R. Vilaseca, Dynamics of Lasers, VCH, New York, 1991.

[2]. L. A. Lugiato, F. Prati, L.M. Narducci, P. Ru, J.R. Tredicce, and D.K. Bandy, Phys. Rev. A 37, 3847 (1988).

[3]. L.A. Lugiato, G.L. Oppo, J.R. Tredicce, L.M. Narducci, and M.A. Pernigo, J. Opt. Soc. Am. B 7, 1019 (1990).

[4]. M. D. Wei, W. F. Hsieh, and C.C. Sung, Opt. Commun. 146, 201 (1998).

[5]. C. H. Chen, M. D. Wei, and W. F. Hsieh, J. Opt. Soc. Am. B 18, 1076 (2001).

[6]. C. H. Chen, P. T. Tai, M. D. Wei, and W. F. Hsieh, J. Opt. Soc. Am. B 20, 1220 (2003).

[7]. C. F. Maes and E. M. Wright, Opt. Lett. 29, 229 (2004).

[8]. H.H. Wu and W.F. Hsieh, J. Opt. Soc. Am. B 18, 7 (2001).

[9]. C.H. Chen, P.T. Tai, W.F. Hsieh, Appl. Opt. 43, 6001 (2004).

[10]. H. Lin and N.B. Abraham, Opt. Commun. 79, 476 (1990).

[11]. E.J. D_Angelo, C. Green, J.R. Tredicce, N.B. Abraham, S. Balle, Z. Chen, and G.L. Oppo, Physica D 61, 6 (1992).

[12]. L. A. Lugiato, C. Oldano, and L. M. Narducci, J. Opt. Soc. Am. B 5, 879 (1988).

[13]. C. Tamm, Phys. Rev. A **38**, 5960 (1988).

[14]. J. R. Tredicce, E. J. Quel, A. M. Chezzawi, C. Green, M. A. Pernigo, L. M. Narducci, and L. A. Lugiato, Phys. Rev. A **62**,1274 (1989).

[15]. G. Slekys, K. Staliunas, M. F. H. Tarroja, and C. O. Weiss, Appl. Phys. B: Lasers Opt. **59**, 11 (1994).

[16]. M. Brambilla, L. A. Lugiato, V. Penna, F. Prati, C. Tamm, and C. O. Weiss, Phys. Rev. A **43**, 5114 (1991).

[17]. P. Colet, M. San Miguel, M. Brambilla, and L. A. Lugiato, Phys. Rev. A **43**, 3862 (1991).

[18]. E. Louvergneaux, G. Slekys, D. Dangoisse, and P. Glorieux, Phys. Rev. A 57, 4899 (1998).

Chapter 4 Laser patterns around degenerate cavity: optical bottle beams

Optical tweezers [1] is a useful technique to manipulate micro-particles and biological samples such as DNA's. Based on similar technique, atoms can also be trapped in use of dipole force [2]. If the trapping beam is blue-detuned from the resonant transition of the atoms, the atoms will seek dark or the low-field region so that the field distribution will not substantially be disturbed by the presence of atoms. Thus the storage time can approach the order of one second [3]. The same character of seeking dark can also be applied to the micro-particles that have lower refractive index than the surrounding medium [4].

An optical bottle beam has a low-intensity zone surrounded by a high intensity shell [5-8]. It had been generated by using a hologram constructed with Laguerre-Gaussian LG_{00} and LG_{20} modes that destructively interferences at their beam waists. Here the first subscript index of LG modes is the radial mode index and the second one is the angular mode index. Recently, we have shown that a bottle beam can be generated from a simple laser near the 1/3 transverse degeneracy but the laser beam consists of many degenerate LG modes being in-phase at the beam waist [9]. In this chapter, we experimentally demonstrate that various optical bottle beams can be generated from a simple laser when it is operated with the degenerate cavities. Moreover, good-contrasted optical bottles can be achieved by controlling the

sizes of pump laser and of an intracavity aperture.

4.1 Motivation

We first show in Figs. 4-1(a) and 1(b) the differences of the bottle beams with destructive and constructive interference of LG_{00} and LG_{20} modes at the beam waist with its width W_0. We see that there are two optical bottles ahead and behind the waist in Fig. 4-1(b) due to Gouy phase shift, while only one bottle of destructive interference located at the waist in Fig. 4-1(a). The beam with two bottles of Fig. 4-1(b) form a double-well potential for blue-detuned cold atoms, so that it may be useful for investigating the interaction between two groups of cold or even Bose-Einstein condensate atoms [10]. We show the three-dimensional potential wells in the right column of Fig. 4-1. Note that the potential wells are plotted only from 0 to $3W_0$ in the radial direction and the fundamental beam waists are assumed to be the same in Figs. 4-1(a)~1(d). The depth of potential well that is proportional to the beam intensity is shallower in Fig. 4-1(b) than that is in Fig. 4-1(a), but the deeper and the narrower potential wells can be constructed by using LG_{00} and LG_{30} modes as well as LG_{00} and LG_{50} modes as shown in Fig. 4-1(c) and 1(d), respectively. We will show in the following that these bottle beams of Figs. 4-1(b)~1(d) can be directly generated from a simple laser near the transverse degeneracies of 1/4, 1/3 and 1/5, respectively.

Considering the simplest two-mirror cavity with the specified mirror curvatures R_1, R_2 and the effective cavity length L, the resonance frequencies of the longitudinal-plus-transverse modes can be given by

$\nu_{m,n,q}=q\nu_l+(m+n+1)\nu_t$, where $\nu_l=c/2L$ is the longitudinal mode spacing, $\nu_t=(\nu_l/\pi)\arccos[(g_1g_2)^{1/2}]$ is the transverse mode spacing, q is the longitudinal mode number, m and n are the transverse mode numbers, and $g_{1,2}= 1- L/R_{1,2}$ being the cavity parameters, respectively [11]. The configurations g_1g_2 = 1/4, 1/2 and $(1+\sqrt{5})^2/16$ corresponding to ν_t/ν_l =1/3, 1/4 and 1/5 will be denoted as 1/3-, 1/4- and 1/5-degenerate configurations, respectively. From previous discussion in the section 3.3, we know that the supermode observed at degeneracy is consist of the in-phase degenerate transverse modes. In our previous studies [9, 12], we have shown that an end-pumped Nd:YVO_4 laser by a small Gaussian pump beam will result in multi beam-waist (MBW) mode as it is operated at degenerate resonator configurations. From Fig. 1-3, we can observe an optical bottle between two beam waists. However, the contrast between dark center and barrier of the optical bottles were not so good as Fig. 4-1(c) because many degenerate eigenmodes are simultaneously excited near the 1/3-degenerate cavity. Furthermore, unequal mode weightings will lead to a non-perfect destructive interference bottle with non-zero on-axis intensity even when the proper eigenmodes are selected, for example, only LG_{00} and LG_{30} modes being excited. However, we can control the sizes of pump beam and an intracavity aperture in the end-pumped Nd:YVO_4 laser to obtain good bottle beams as depicted in Figs. 4-1(b)-1(d).

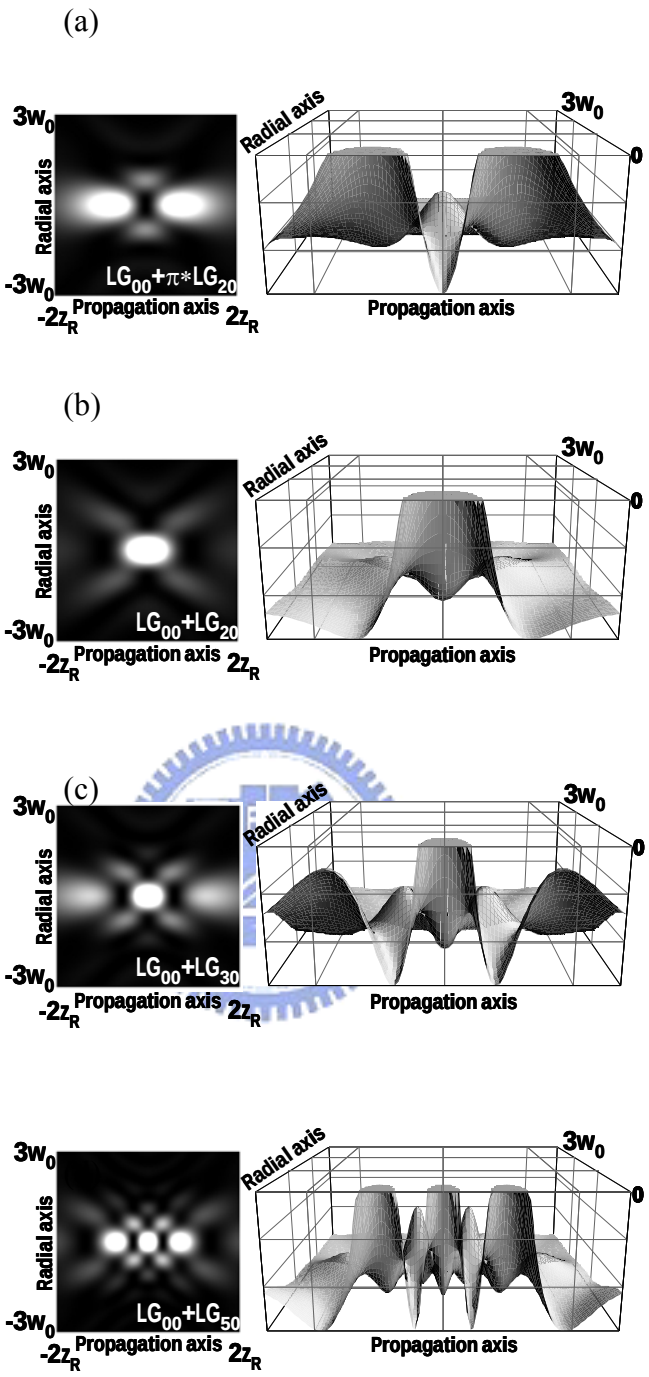

Fig. 4-1 Intensity patterns and their corresponding three-dimension profiles. (a) out-of-phase summing up LG_{00} and LG_{20} modes at beam waist, (b~d) in-phase adding LG_{00} and LG_{20}, LG_{00} and LG_{30}, as well as LG_{00} and LG_{50} modes, where the W_0 is the beam waist, and z_R is the Rayleigh length.

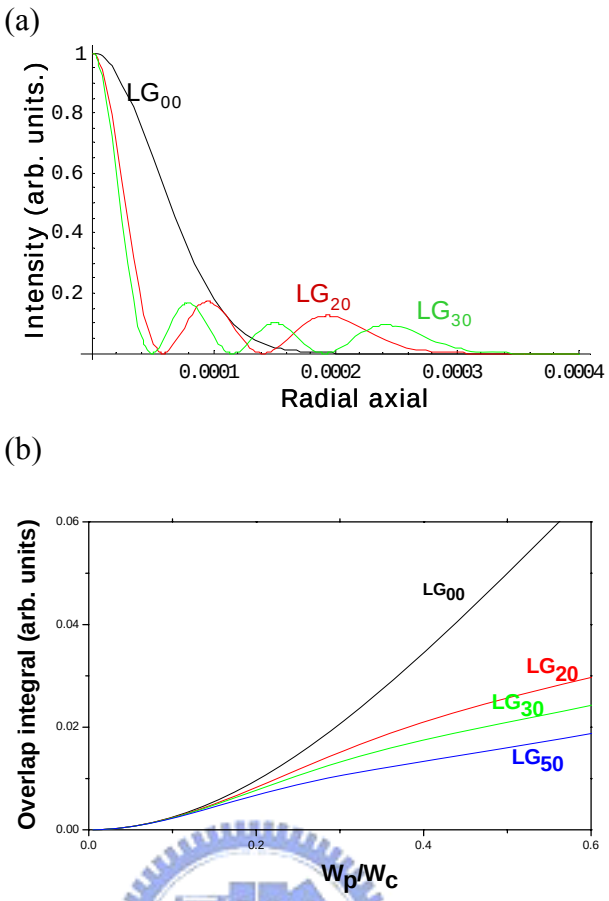

Fig. 4-2 The transverse modes distribution (a) as well as overlap integral of pump spot (W_p) and W_0.

We can use Fig. 4-2 to realize the idea for creating a perfectly bottle beam. The transverse mode distribution is show in Fig. 4-2(a). It can be easily observed that the high-order transverse mode widely distribute with narrow central portion. So we can use a hard aperture to increase loss of high-order mode; and control lasing transverse modes which only contains fundamental and the lowest-order transverse mode. In addition, the narrow central portion indicates that we can use tightly-focused pump spot to increase mode weight of the high-order mode. We show the overlap integral of pump field (W_p) with different transverse modes. The transverse modes will have almost equally value of overlap integral when W_p is small

enough. It tells us small pump spot will increase the mode weight of the high-order mode related to the fundamental mode.

4.2 Experiment setup and discussion

The experimental setup shows as Fig. 4-3. A plano-concave laser cavity contains a 1 mm-thick Nd:YVO_4 crystal and an output coupler with radius of the curvature R_c = 8 cm having 10% transmission at the lasing wavelength of 1.064 μm. One surface of the crystal facing to the pumping beam acts as a flat mirror of the cavity and is dichroically coated with reflection greater than 99.8% at 1.064 μm and transmission greater than 99.5 % at the pump wavelength of 808 nm; and the other surface was anti-reflectively coated at 1.064 μm to avoid intracavity etalons effect. The output coupler was mounted on a translation stage so that we can tune the cavity length around the degenerate configurations where semi-confocal is at L=4cm, 1/3 degeneracy at L=6cm, and 1/5 degeneracy at L=5.2cm. The pump source is a continuous-wave Ti-sapphire laser with TEM_{00} mode. In our experiment we used several pump sizes that were determined by the standard knife method. In order to control the lasing modes, we insert a knife edge into the cavity against the gain medium as a hard aperture that allows the oscillation of mere fundamental mode and a single degenerate transverse mode. For example, the aperture has radius of 300μm on the optical axis for sustaining only LG_{00} and LG_{20} modes in the semi-confocal or 1/4-degenerate resonator.

The Nd:YVO_4 laser output was split into two beams. One of which was used to project the far-field pattern on a screen located at a distance of ~

50cm from the flat mirror; the other beam was propagated through a transform lens (TL) to study beam propagation and then was detected by a Charge Coupled Device (CCD) camera. To image the mode pattern directly behind the TL with less noise, we replaced the camera lens of the CCD by a laser line filter and added some adequate absorptive neutral density filters.

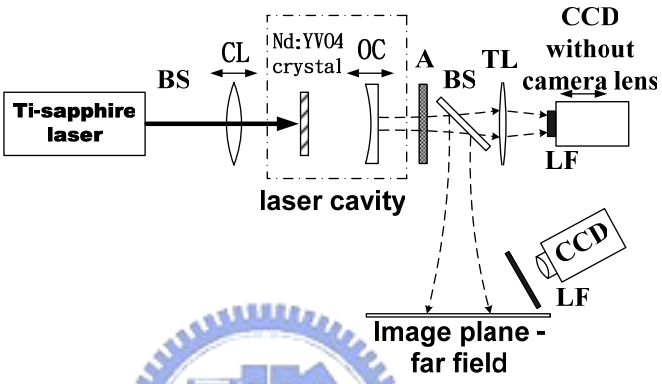

Fig. 4-3 The sketch of experiment setups.

To verify the optical bottles of the above-mentioned modes, we showed in Fig. 4-4 the intensity distribution of the optical bottle along the propagation distance when the laser is operated at 1/4-degeneracy. We have normalized the propagation distance to the Rayleigh length z_R that was indicated above the photographs. The observed optical bottle is ahead of the beam waist at z=0, and its extended range is about $2.36z_R$. Similar but shorter extended regions of optical bottles for the 1/3- and 1/5-degenerates can also be observed due to rapid variation of Gouy phases of LG_{30} and LG_{50}, respectively. Behind the beam waist at z=0 we can also observe a similar optical bottle which is consistent with Fig. 4-1(b)~(d) but appears farther from the waist. However, the double optical bottles of Fig. 4-1(b)-(d)

should appear symmetrically to the beam waist because of symmetrical variation of Gouy phases around the waists. In the experiment, however, we observed unsymmetrical double optical bottles after the transform lens (TL). This can be explained by excess Gouy phase shifts of the higher order transverse modes, and therefore formation both LG_{00} and LG_{p0} images are at different distances. Assume both of LG_{00} and LG_{p0} modes are in-phase at the waist, they experience different Gouy phase shifts while they reach the TL. Looking back through TL, those two modes seem to come from two different point sources because they experience different phase shifts or optical path lengths. Their images therefore will be slightly separated to result in asymmetric double optical bottles. We can bring these two images together again to produce symmetric optical bottles as Fig. 4-1(b)~(d) by using two lenses to collimate at first then focus the collimated beam to form symmetric double optical bottles.

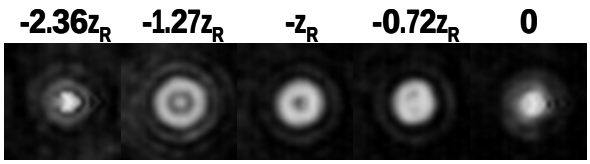

Fig. 4-4 The radial intensity patterns of the optical bottle generated from a laser operated with the 1/4-degenerate cavity at various distances from the transform lens which is indicated above the photographs, where z_R is the Rayleigh range.

Because there are only 30x30 pixels in photographs of Fig. 4-4, the spatial resolution is too low to show the detailed beam character, we expanded the laser beam by 5 times to monitor the radial distribution of the center of various optical bottles. Shown on the right column of Fig. 4-5 are

the photographs of the bottle beams under 300mW pumping with a pump size of 30 μm when the laser is operated at 1/4-degeneracy with an intracavity aperture of 300μm and at 1/3-degeneracy with 350μm aperture, respectively. The parallel streaks on the photographs are caused by interference from the protection window of the CCD. By in-phase summing the LG_{00} and LG_{20} modes for 1/4-degeneracy and the LG_{00} and LG_{30} modes for 1/3-degeneracy at the beam waist (z = 0), we show the calculated optical bottle profiles on the left column of Fig. 4-5 at $z = z_R$ and at $z = z_R/\sqrt{3}$ respectively. We see the excellent agreement between the experiments and the calculations. However, there are about 5% observed residual intensity at the center of the bottle for both of the 1/4- and 1/3-degenerate configurations. It must be mentioned that each pixel of CCD is $7x7\mu m^2$ which may not be able to resolve the region of lowest intensity of only several microns even having been magnified 5 times. The central pixel may detect some energy adjacent to the optical axis and the actual residual intensity should be lower than the measured 5%.

Because the central portion of LG_{50} mode is more localized than that of LG_{00}, LG_{20} or LG_{30}, the smaller pump size can effectively decrease the mode weight of fundamental mode to enhance LG_{50} mode. The higher degenerate configuration tends to generate the narrower and the deeper optical bottle by choosing the smaller beam size to pump this laser. In order to obtain the narrower and deeper optical bottle, we pay our attention to the 1/5-degeneracy. Note that the fundamental mode radius is 113μm in this case. With intracavity aperture of 450μm, we show the experimental results in the Figs. 4-6(a)~4-6(c) for the pump radius of 30, 20, and 15μm respectively,

and in Fig. 4-6(d) is the calculated bottle with LG_{00}+LG_{50} at z = 0.324z_R. Comparing Fig. 4-6(b) with Fig. 4-6(d), we see the bottle with three obvious concentric rings that means the aperture has properly selected only LG_{00} and LG_{50} modes. We also see from Fig. 4-6(a)~4-6(c) that the central intensity decreases from about 13% to 2.5%. We used the smaller pump size of 20 μm for the 1/5-degeneracy instead of using pump size of 30μm for the 1/4-degeneracy and 1/3-degeneracy to achieve the same residue intensity as on the right column of Fig. 4-5. This means that the mode weighting can be experimentally controlled by the pump radius. A small pump size gives the mode weight ratio approaching to 1 which leads to optical bottle with good contrast.

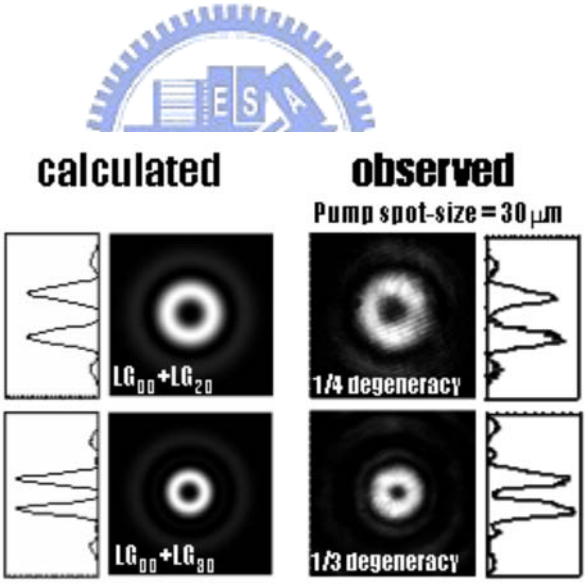

Fig. 4-5 The calculated radial intensity distributions and the experimentally observed beam profiles. The calculated transverse profile of LG_{00}+LG_{20} is at z = z_R and of LG_{00}+LG_{30} at z = zR/$\sqrt{3}$ that correspond to the photographs taken at 1/4- and 1/3-degeneracy, respectively.

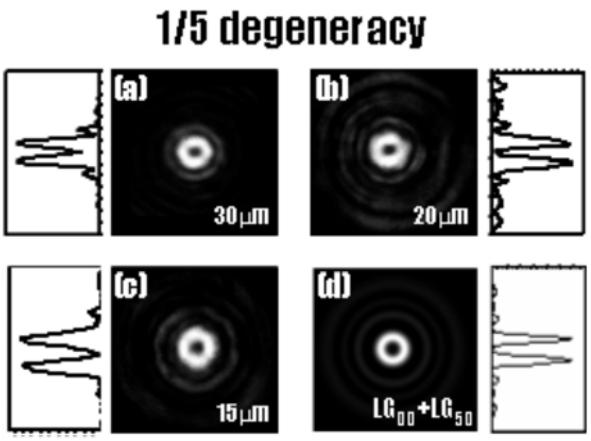

Fig. 4-6 The depth of optical bottle versus different pumping size and corresponding calculated profiles at 1/5-degeneracy. The CCD images in (a)~(c) are the beam patterns when the laser is operated with pump size of 30μm, 20μm, and 15μm respectively. (d) The calculated profile of $LG_{00}+LG_{20}$ is at $z = 0.324\ z_R$

One may ask questions that practically how to ensure the laser is operated at the degeneracy and how to properly determine the aperture size? We will discuss these experimental details in the following. Because the Gouy phase difference of LG_{00} and LG_{50} modes is 5π at the far field where the profile exhibits a dark center as show in Fig. 4-7, we can easily identify the point of 1/5 degeneracy where the laser has the lowest threshold. And, in the Fig. 4-7, by counting number of the concentric rings we can identify whether the aperture size is proper, for example, a single concentric ring for $LG_{00}+LG_{20}$, two rings for $LG_{00}+LG_{30}$, and three rings for $LG_{00}+LG_{50}$. In addition, one can focus the pumping beam near the rim of the crystal instead of actually placing a real aperture against the crystal inside the cavity.

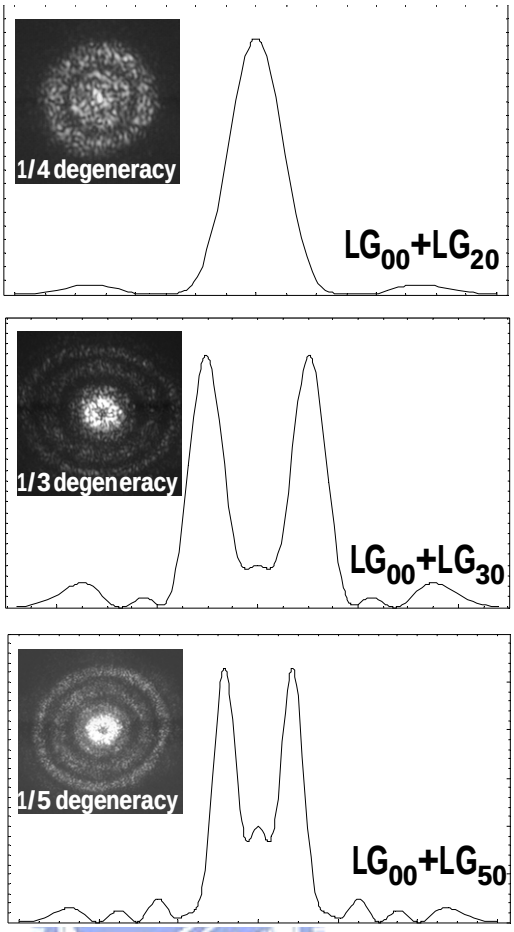

Fig. 4-7 Photographs of the far-field patterns by the laser operated at semi-confocal, 1/3, and 1/5 degenerate configurations. The hard aperture is 300μm, 350μm, and 430μm, respectively. The corresponding calculation profiles are plotted by in-phase summing up the fundamental and the lowest degenerate transverse mode.

Optical bottle beam have been generated in use of holograph [5], spatial light modulator [6], and two beam interference [3, 8]. Those methods need enormous calculation to prepare a suitable holograph with low conversion efficiency, or well control of phase retardation for each pixel of SLM and two overlapped beams to make the destruction interference occurring at the beam center. Our method of generating the bottle beams directly from a simple laser may be convenient for some applications. The demonstration of the Nd:YVO_4 laser in this experiment that emits at wavelength of 1064nm may

not be suitable for blue-detuned light trap of atoms. However, in use of the Collins integral together with rate equation to study pattern formation and laser dynamics as stated in the previous study [9, 12], and we found that the bottle beam from a laser is independent of the active medium as long as it satisfies the thin slab approximation and the homogeneous 4-level assumption. If only the pump size is properly controlled smaller than the beam waist of the fundamental mode of the cavity and an aperture is introduced to eliminate unwanted high order modes, an optical bottle beam with double wells results from cooperative frequency locking of the lowest two degenerate transverse modes. Therefore, one can choose an appropriate gain medium and employ with the degenerate cavity configurations to generate bottle laser beam for trapping atoms in the dark field.

4.3 Conclusion

In conclusion, we have demonstrated direct generation of various optical bottle beams from the degenerate cavity configurations in a compact solid state laser in use of appropriate pumping size and aperture. In particular, the good optical bottle is achieved with the superposition of LG_{00} and LG_{50} modes from the 1/5-degenerate cavity. This new scheme of generating bottle beams from end-pump solid-state lasers may be applied for optical atom trap.

References

[1]. Ashkin, J. M. Dziedzic, J. E. Bjorkholm, and S. Chu, Opt. Lett. **11**, 288 (1986).

[2]. R. Grimm, M. Weidemuller, and Y. B. Ovchinnikov, Adv. At. , Mol., Opt. Phys. **42**, 95 (2000).

[3]. R. Ozeri, L. Khaykovich, and N. Davidson, Phy. Rev. A **59**, R1750 (1999).

[4]. K. T. Gahagan, and G. A. Swartzlander, Opt. Lett. **21**, 827 (1996).

[5]. J. Arlt, and M. J. Padgett, Opt. Lett. **25**, 191 (2000).

[6]. D. McGlin, G. C. Spalding, H. Melville, Opt. Commun. **225**, 215 (2003).

[7]. T. Freegarde, and K. Dholakia, Phy. Rev. A **66**, 013413 (2002).

[8]. D. Yelin, B. E. Bouma, and G. J. Tearney, Opt. Lett. **29**, 661 (2004).

[9]. H. Chen, P. T. Tai, and W. F. Hsieh, Appl. Opt. 43, 6001 (2004).

[10]. Y. Shin, M. Saba, A. Schirotzek, T. A. Pasquini, A. E. Leanhardt, D. E. Pritchard, and W. Ketterle, Phy. Rev. Lett. **92**, 150401 (2004).

[11]. E. Siegman, *Laser* (University Science Books & Sausalito, CA, 1986), Chap. 19.

[12]. H. Chen, P. T. Tai, W. F. Hsieh, and M. D. Wei, J. Opt. Soc. Am. B **20**, 1220 (2003).

Chapter 5 Optical spectrum around the degenerate cavity: Suppression of spatial hole burning

The single-frequency laser is essential for stable operation of intracavity frequency doubling, precision measurement, high-resolution spectroscopy, and laser trapping or cooling. The most common method of obtaining single-frequency operation in a homogeneously broadened solid-state laser is to build a traveling wave cavity, usually by means of a ring cavity with an intracavity optical diode so as to prevent the spatial hole-burning effect. To acquire single-frequency operation in a linear cavity, however, some ways are required to diminish the spatial hole-burning effect. For example, a twisted mode technique [1] had been proposed to achieve uniform energy density along the optical axis of the laser cavity. In addition, the mechanisms of Auger upconversion and energy diffusion in the laser crystal were also employed to reduce the spatial hole-burning effect [2-4].

Recently, it was shown that a plano-concave cavity with the degenerate resonator configuration could support arbitrary beam distribution. Under tightly focused pump beam, the laser exhibits shrinking beam waist and the lower pump threshold than the neighboring configurations [5, 6]. In this Chapter, we will report a novel way by employing the degenerate resonator

configuration to relief the spatial hole-burning effect. Because the laser with a degenerate resonator configuration is capable of self-adjusting its mode distribution to match the small pump beam, very high intensity is able to attain in the gain medium. Most of the gain, therefore, can be depleted even by a standing wave field. The spatial hole-burning effect is then effectively suppressed. This was numerically simulated in terms of a spatial dependent rate equation and experimentally demonstrated by using a Nd:YVO_4 laser discussed previously. The Nd:YVO_4 laser crystal has high absorption coefficient which is a merit for single-frequency operation in a standing-wave cavity, but the pump power is usually limited to slightly above the threshold [7]. Our method, however, is capable of suppressing the spatial hole-burning effect beyond 20 times the pump threshold.

5.1 Theoretical model and simulation

In order to investigate the spatial hole-burning effect in a plano-concave Nd:YVO_4 laser, we employ a spatial dependent rate equation. By taking into account both the Auger upconversion and energy diffusion effects, the rate equation for the density of population inversion $N(z)$ in an ideal four-level system can be expressed as [2, 4, 8]

$$\tau \frac{\partial}{\partial t} N(z) = \tau R(z) - \left(1 + \frac{I(z)}{I_s}\right) N(z) + \tau D\left(\frac{\partial^2 N(z)}{\partial z^2}\right) - A\tau N^2(z), \qquad (5.1)$$

where z is the cavity axis with z = 0 at the flat mirror, $R(z)$ is the pump rate, I_s is the saturation intensity, τ is the spontaneous emission lifetime, D is the diffusion constant, and A is the Auger upconversion coefficient, respectively. Assuming a low roundtrip loss in the plane wave approximation, we can write the intensity $I(z)$ of standing wave as

$$I(z) = 4I_0 \sin^2(kz), \tag{5.2}$$

where k is the propagation wavenumber and I_0 is the average intracavity intensity. Because we do not consider the radial effect in Eq. (5.1), the pump rate can be written as

$$R(z) = \frac{P_p}{h\nu \times \pi w_p^2} \times \frac{e^{-\alpha z}}{\alpha}, \tag{5.3}$$

where P_p is the incident pump power, h is the Planck's constant, ν is the pump frequency, w_p is the pump size, and α is the absorption coefficient at pump wavelength. Under the steady-state condition, we substituted Eqs. (5.2) and (5.3) into (5.1), and numerically solved the equation by the Newton's method to obtain the spatial profile of $N(z)$. The Auger upconversion coefficient A = $3\text{x}10^{-21}$ m^3/s [4, 8], diffusion constant D = $0.7\text{x}10^{-11}$ m^2/s [4], absorption coefficient $\alpha = 31.4$ cm^{-1}, and saturation intensity $I_s = 1.19\text{x}10^7$ $J/(m^2s)$ are used in our simulation.

Usually the laser is expected to operate at the single longitudinal mode when the pump power is just above the threshold. From the Ref. 7, we estimate that the second longitudinal mode would begin to oscillate at γ = 1.78, where γ is the ratio of pump power to laser threshold, therefore, we will discuss the numerical results using the pump power around γ = 1.78. Because the thickness of the laser crystal is less than the Rayleigh parameter of the pump beam, we assume that the pump size w_p is constant throughout the crystal. When a laser operates in the vicinity of g_1g_2 = 1/4 with a spherical of 8-cm radius, the radius of the fundamental transverse mode is about 108μm. It corresponds to Rayleigh parameter of about 34 mm which is much longer than the length of gain medium of 1 mm. In addition, the

plane wave assumption is adequate for a beam having or close to Gaussian profile. Note that the laser beam spot in the vicinity of flat mirror (gain medium) is almost equal to the pumping size of $w_p = 20$ μm and is similar to Gaussian profile [5] when it is operated with the degenerate resonator configuration under tightly-focused pumping. The plane wave assumption in Eq. (5.2) is still valid even with the high-order Laguerre-Gaussian mode up to $LG_{12,0}$, whereas, the shrinkage of beam spot can be observed at the degeneracy with only a superposition of LG_{00} and the lowest degenerate mode, e.g., $LG_{3,0}$ for $g_1g_2=1/4$ [13].

Figure 5-1(a) is the spatial profile of N(z) for a laser operated at cavity length L = 6.06cm which is a typical example of population inversion in a standing wave resonator. It only burns a small hole of N(z) at anti-node of standing wave and leaves sufficient gain for the second longitudinal mode to lase. The horizontal dash line in this figure stands for the threshold population inversion with pump power of 33 mW, the solid and dash curves respectively show $N(z)$ for the laser operating at $\gamma_c = 1.5$ and $\gamma_c = 2.4$, where the subscript c denotes the conventional cavity. To allow the second mode to oscillate ($\gamma_c > 1.78$), the residual population inversion should higher than that for the laser operating at $\gamma_c = 1.5$ as shown in Fig. 5-1 (a).

If we operate the laser at the degenerate resonator configuration where $g_1g_2 = 1/4$ (L = 6.0 cm), good overlapping between the pumping and the laser beam will result in a lower laser threshold which equals to 15mW. The beam radius will be about 20 μm which approximates to the size of pump. The intracavity intensity at the beam waist (z = 0) is about 29 times higher than that of the laser with the conventional cavity (L = 6.06-cm). Because

of the very high intracavity intensity, there leaves only a little residual population inversion above the threshold which is located around the node of the standing wave, as shown in Fig. 5-1(b). The horizontal dash line again stands for the threshold population inversion.

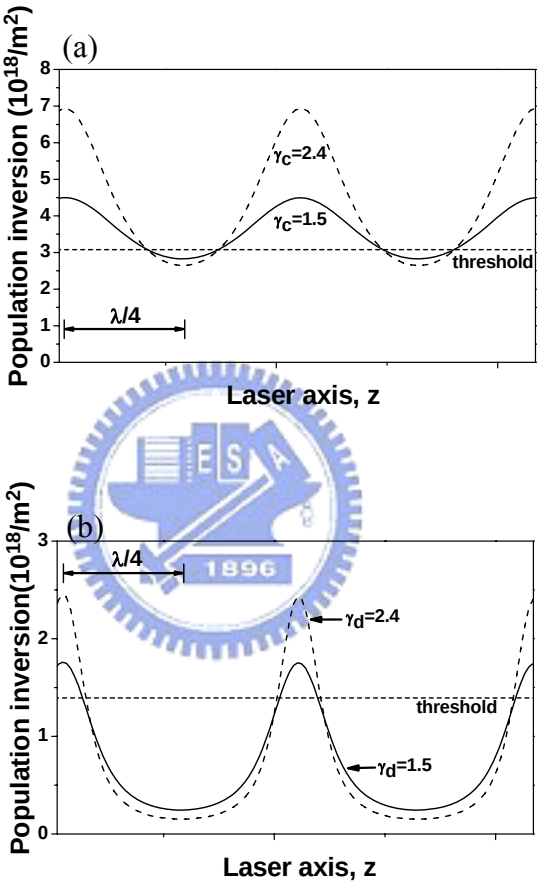

Fig. 5-1. Numerical spatial distribution of steady-state upper level density to show influence of spatial hole-burning effect. The normalized pumping γ (to the threshold) for both of the conventional laser operated at L=6.06cm (a) and bottle beam laser at g_1g_2=1/4 (b).

Other longitudinal modes could have significant access to the residual inversion only if they had at least $\pi/2$ phase shift relative to the first mode [7]. Two lasing frequencies, which is in-phase at beginning, will possess $\pi/2$

phase difference after propagating a dephasing length. Usually the first lasing mode in a homogeneously broadened gain medium is located near the center of gain profile, and the shortest dephasing length is provided by the maximum frequency difference. So we used half of bandwidth to estimate the shortest dephasing length to be 700μm. This implies that the other longitudinal mode needs more than 2.3 times absorption depth of Nd:YVO_4, which is reciprocal of absorption coefficient α, to extract enough residual gain to oscillate. From Fig. 5-1(b), we see that the residual population inversion for $\gamma_d = 1.5$, where the subscript d denotes the degenerate cavity, is too small to allow oscillation of the second mode. Nevertheless, for $\gamma_d = 2.4$ or even the higher pump power, because the higher residual population inversion occurs at the nodes of the standing wave, the second mode still can not obtain the sufficient gain. In addition, it is worth to mention that by neglecting the energy diffusion and Auger upconversion effects, the last two terms of the right-hand side of Eq. (5.1), we still obtained the similar numerical results of Fig. 5-1(b). This implies that the effects of Auger upconversion and the energy diffusion are negligible and can be ruled out in our case. Therefore, we conclude that the laser with the degenerate resonator configuration is capable of suppressing the spatial hole-burning effect by means of gain saturation through the very high intensity in the gain medium.

5.2 Experiment setup and results

In order to confirm our numerical calculation, the experiment is performed in a Nd:YVO_4 laser with a plano-concave cavity. The detail

setup similar to the previous Chapters is show in Fig. 5-2. A photodetector (rise time < 0.3 ns) together with a RF spectrum analyzer (HP8560E, bandwidth 2.9 GHz) was used for measuring the mode beating and the relaxation oscillation. The optical spectrum was measured by using a Fabry-Perot interferometer (FPI, Burleigh) having finesse > 150 corresponding to a spectral resolution of 100 MHz for a 15 GHz free spectral range (FSR). In addition, the pump size determined by the standard knife-edge method is 20 μm, which is less than one-fifth of the waist radius (108 μm) of the cold cavity mode. The cavity length corresponding to the degenerate resonator configuration is determined by minimum pump threshold [6]. In this experiment, we operated the laser around the 1/3-degeneracy (L = 6 cm), which corresponds to the longitudinal mode spacing of about 2.4 GHz.

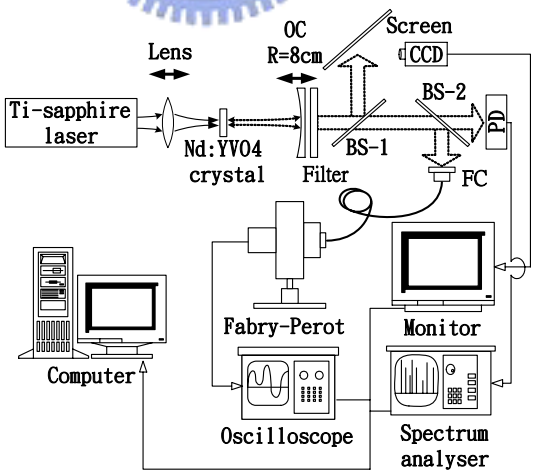

Fig.5-2 The sketch of experiment setups.

Figure 5-3 shows a typical single-frequency optical spectrum measured by FPI when the laser is operated at $\gamma < 1.8$ (~ 1.78) in the conventional

cavity configuration (L = 6.06 cm). The second longitudinal mode appears when $\gamma_c = 1.8 > 1.78$ (threshold is 33 mW). The experiment observation agrees well with the theoretical estimation according to the Ref. 7. Figure 5-4 (a) and (b) respectively show the FPI and the RF spectra for $\gamma_c = 2.7$ (pumping power P_p = 90 mW). We can clearly see the second longitudinal mode and the beating from these two longitudinal modes. As the pump power increases to over 133 mW ($\gamma_c = 4$), we found that an extra lasing mode appears at 1.1 GHz away from the main features of the FPI spectrum but no corresponding mode beating can be detected by the RF spectrum analyzer. Therefore, we suspected that the spectral spacing of these two lasing modes is larger than the bandwidth of the RF spectrum analyzer (2.9 GHz). Indeed, when the FPI with larger FSR (150 GHz or even 300 GHz) is used, the measured mode spacing becomes 40 GHz.

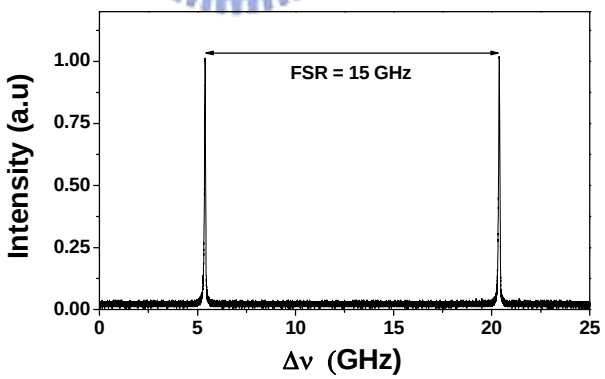

Fig. 5-3 Single frequency optical spectrum of the Fabry-Perot interferometer with FSR = 15 GHz when the pumping is set below 1.8 times threshold.

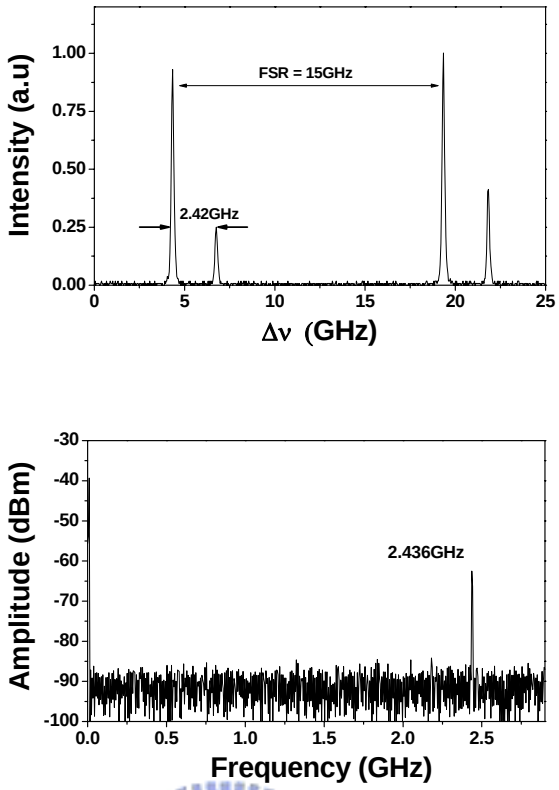

Fig. 5-4 Typical multiple optical frequency and corresponding RF spectrum for the common laser at L=6.06cm. (a) The Fabry-Perot interferometer shows two longitudinal lasing modes with spacing of about 2.42 GHz and (b) the beat frequency of two longitudinal modes measured by the RF analyzer.

On the other hand, as the cavity is adjusted to the degenerate resonator configuration (L = 6 cm), the single frequency operation is observed, as shown in Fig. 5-3, for the pump power as high as 30 mW. By raising the pump power to above 30 mW ($\gamma_d = 2$), we found that the second mode appear in the FPI spectrum which is located 58.6 GHz away from the first mode rather than ~2.4 GHz. The next nearest neighboring longitudinal mode is not observed even the pumping power increases as high as we can. The FPI and the corresponding RF spectrum at $P_p = 310$ mW or $\gamma_d \sim 20$ are shown in the Fig. 5-5(a) and (b) respectively. The inset of Fig. 5-5(b) shows that there is neither longitudinal nor transverse mode beating within the

bandwidth of the RF spectrum analyzer, the arrow in this figure shows only one relaxation oscillation peak (2.4 MHz) existing in the RF spectrum. One may doubt whether the mode spacing of 58.6 GHz comes from the intracavity etalon effect. We estimated the mode spacing resulting from etalon effect of 1mm-gain medium is 72 GHz; in addition, there is an antireflection coating at 1064 nm on the Nd:YVO_4 facet to avoid the effect of intracavity etalons.

As the simulated results discussed in the previous section, the laser with the degenerate resonator configuration is able to deplete most of the population inversion in a homogeneous broadened gain medium. We therefore expect that the second mode 58.6 GHz away from the first mode may have different origin of emission or arise from different manifold of transition (sub-peak of inhomogeneous gain profile). Similarly, the sub-peak of the gain profile will also result in occurrence of the second mode in the conventional cavity at higher pump power, which is 40 GHz away from the first mode. In the Nd:YVO_4 crystal, the crystal field interaction gives rise to the Stark splitting at the satellite of $^4F_{3/2}$, $^4I_{9/2}$, and $^4I_{11/2}$ [9]. Under high-resolution absorption and luminescence studies, it was found that the satellite energy of $^4F_{3/2} \rightarrow {}^4I_{9/2}$ transition depended on the Nd^{3+} concentration [10]. The lasing transition around 1064 nm is attributed to $^4F_{3/2} \rightarrow {}^4I_{11/2}$. It contains two closely transitions $R_1 \rightarrow Y_1$ and $R_2 \rightarrow Y_2$ with frequency difference of 90 GHz under 2% Nd^{3+} doping and 21 GHz under 0.56% Nd^{3+} doping [11, 12]. The doping concentration used in our experiment is 1%, it is quite reasonable to obtain the frequency difference of ~42 GHz by simple interpolation. The frequency difference which is

estimated by interpolation is in good agreement with our observation in the conventional laser cavity. Note that because the second mode has a frequency more than 40 GHz away from the first mode, it would be easily filtered out, for example, by a grating with 1800 grooves/mm. In principle, it is possible to design a cavity that delivers the same tight beam size in a fundamental TEM_{00} mode and achieve the same effect. However, such a cavity is usually operating close to the edge of stability and needs to accurately adjust the cavity length according to the spot size of the pump beam. Our scheme, in contrast, is operated within the stability region away from the edge of stability. Without knowing the pump beam size in advance, the laser with a degenerate resonator configuration can self-adjust the mode distribution to match the small pump beam and as a result the spatial hole-burning effect is suppressed.

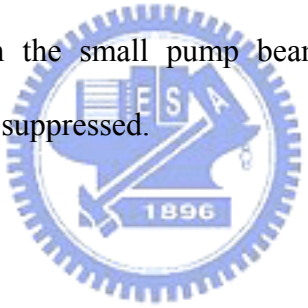

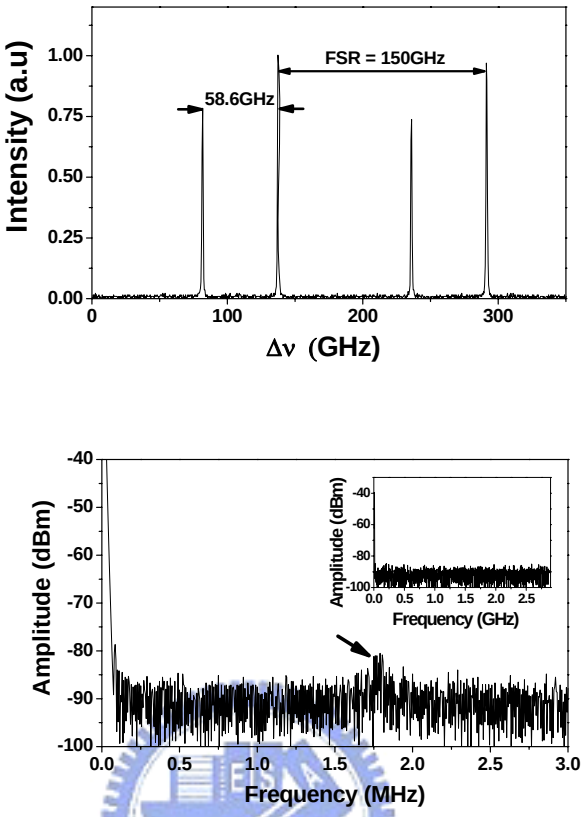

Fig. 5-5 Multiple optical frequency and corresponding RF spectrum under 310mW pumping at g_1g_2=1/4. (a) The FPI spectrum shows mode spacing of about 58.6GHz but without longitudinal beating of 2.42 GHz or transverse mode beating in the RF spectrum in (b). An arrow points out the peak due to relaxation oscillation.

5.3 Conclusion

We have theoretically shown and experimentally demonstrated that the spatial hole-burning effect can be suppressed by using a plano-concave cavity with degenerate resonator configuration under a tightly focusing pump beam. It not only has the merits of the lowest threshold and stable output but also is independent of the gain medium. The same resonator configuration has been employed to generate the multiple beam waists and

the optical bottle beam [13, 14], it has potential applications for trapping atoms in the dark field if the proper gain medium is chosen to generate blue-detuned single frequency laser beam.

References

[1]. V. Evtuhov and A. E. Siegman, Appl. Opt. **4**, 142 (1965).

[2]. K. Otsuka and K. Kubodera, IEEE J. Quantum Electron. **QE-16**, 538 (1980).

[3]. K. Otsuka, P. Mandel and E. A. Viktorov, Phy. Rev. A, **56**, 3226 (1997).

[4]. L. Meilhac, G. Pauliat and G. Roosen, Opt. Commun. **203**, 341 (2002).

[5]. C. H. Chen, P. T. Tai, M. D. Wei, and W. F. Hsieh, J. Opt. Soc. Am. B **20**, 1220 (2003).

[6]. H. H. Wu and W. F. Hsieh, J. Opt. Soc. Am. B **18**, 7 (2001).

[7]. G. J. Kintz and T. Baer, IEEE J. Quantum Electron. **26**, 1457 (1990).

[8]. Y. F. Chen, C. C. Liao and S. C. Wang, Appl. Phys. B **70**, 487 (2000).

[9]. J. R. O'Connor, Appl. Phys. Lett. **9**, 407 (1966).

[10]. Guillot-Noel, V. Mehta, B. Viana, D. Gourier, M. Boukhris, and S. Jandl, Phys. Rev. B, **61**, 15338 (2000).

[11]. D. K. Sardar and R. M. Yow, Opt. Matter. **14**, 5 (2000).

[12]. F. J. Manjon, S. Jandl, G. Riou, B. Ferrand, and K. Syassen, Phys. Rev. B, **69**, 165121 (2004).

[13]. P. T. Tai, C. H. Chen, and W. F. Hsieh, Opt. Express **12**, 5827 (2004).

[14]. C. H. Chen, P. T. Tai, and W. F. Hsieh, Appl. Opt. **43**, 6001-6006 (2004).

Chapter 6 Conclusion and Future works

6-1 Laser dynamics

We use numerical model and experimental to investigate a tightly-focused end-pumped Nd:YVO_4 laser which operates in the vicinity of degenerate cavity configurations. The cylindrically symmetric model which clearly indicates the location of self-pulsation, the reasons why we observe the temporal or spatiotemporal dynamics respectively in instability region of short- or long-cavity side, and the influence of thermal lens agrees well with results of experiment. However, if we want to observe the route to chaos by simulation, we need scaling 5 times the spontaneous emission rate. It indicates that there are something will influence the spontaneous emission rate in experiment. Using simple linear stability analysis of single-mode laser, the relaxation oscillation depends on the spontaneous emission rate which shows as [1]

$$2\pi \times f_{sp} = \sqrt{\frac{(\gamma - 1)}{\tau_f \tau_c}}, \tag{6.1}$$

where f_{sp} is relaxation oscillation frequency, γ is the normalized pumping power, τ_c is the photon lifetime, and τ_f is the atom lifetime which equals to reciprocal of spontaneous emission rate. The Nd:YVO_4 is class B laser whose the polarization lifetime of atom is much shorter than τ_c. In such a

oscillator, the photons and population inversion are coupled and the perturbations, such as white noise, will exhibit relaxation oscillation [2-3]. We can use RF-spectrum to measure relaxation oscillation versus pumping. The experiment results are show in Fig. 6-1. We use Eq. 6.1 to fit the experiment data and find that the τ_f=33μs in degenerate cavity is the smallest which corresponds to the highest spontaneous emission rate. However, the life time of Nd:YVO_4 is 90 μs which is indicated by the specification, as shows in the numerical result of Fig. 6-1. It means that we indeed observe the spontaneous emission rate speeds up.

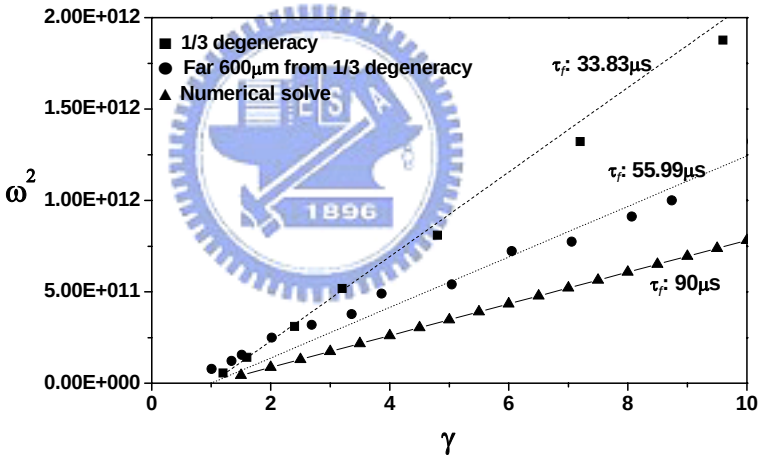

Fig. 6-1 The relaxation oscillation versus normalization pumping power. The solid square and circular are represent the experiment results at 1/3 degeneracy and far 600μm from 1/3 degeneracy, respectively. The solid triangle is the numerical solution.

What physical parameters can control instability is very import in laser dynamics. Although the speeding-up spontaneous emission rate will let the self-pulsation from period to chaos, we always treat the spontaneous emission rate as an inherent process. It means that the spontaneous

emission of atoms will be independent of the environment. However, from our knowledge, the additional process in the upper level density, such as cavity QED or Auger upconversion [4-8], will speed up the spontaneous emission rate. Therefore, we can use experiment to determine it in the future.

6.2 Laser linewidth

In the observations of experiment and mode expansion by method of GA, we know that frequency locking of the transverse mode is presented around the degenerate cavities. The frequency locked supermode which will shrink its beam waist to fit with pumping beam in turn the spatial hole burning is suppressed in a standing-wave resonator. Because the spatial hole burning is suppressed, a single-frequency laser can be easily obtained at degeneracy with tightly focused pump for some applications, such as precision measurement, high-resolution spectroscopy, and laser trapping or cooling. In these applications, the linewidth of laser must be considered. Therefore we can compare the linewidth of locking mode with the single mode laser.

Recently, Maes and Wright [9-10] found that the Petermann K factor is cavity-configuration-dependent near the degenerate cavity configurations in a geometrically stable cavity with Gaussian gain. The K factor first introduced by Petermann [11] for gain-guided laser systems, describes the enhancement of the quantum-limited laser linewidth. We can easily realize that the large K factor results in wider linewidth. Therefore it can be imaged that the linewidth of laser light will depend on the cavity

configuration around degeneracy.

6.3 Optical trapping

Conventionally optical tweezers [12] use tightly-focused Gaussian beam to trap micro-particles which have higher refractive index than surround medium. However, this technical can not trap low-index micro-particles. Because high intensity area will provide a potential barrier for a low-index particle [13], the trapping beam must have low-intensity zone surrounded by a high-intensity shell. This beam is called as optical bottle beam [14].

In our experiment, we can utilize different degenerate cavities to generate various optical bottle beams; the optical bottles are formed before and behind the beam waist. It is must be noted that the beam waist still maintains highly concentrated light spot. The optical bottle beam which produced in our experiment can trap high-index particles by the beam waist and trap low-index particles by the optical bottles. Therefore, we can manipulate any kinds of micro-particles by the single beam. It will very useful for the optical trapping.

References

[1]. E. Siegman, Laser (Mill Vally, CA, 1986).

[2]. C. O. Weiss and R. Vilaseca, Dynamics of Laser (VCH, NY, 1991)

[3]. K. Otsuka, P. Mandel, and E. A. ViktoroV, Phys. Rev. A 56, 3226 (1997).

[4]. K. Otsuka, and K. Kubodera, IEEE J. Quantum Electron. QE-16, 419 (1980).

[5]. K. Otsuka, and K. Kubodera, IEEE J. Quantum Electron. QE-16, 538 (1980).

[6]. D. J. Heinzen, and M. S. Feld, Phys. Rev. Lett. 59, 2623 (1987).

[7]. D. J. Heinzen, J. J. Childs, J. E. Thomas, and M. S. Feld, Phys. Rev. Lett. 58, 1320 (1987).

[8]. Y. Yamamoto, S. Machida, Opt. Quantum Electron. 24, S215 (1992).

[9]. C. F. Maes, and E. W. Wright, Opt. Lett. 29, 229 (2004).

[10]. C. H. Chen, P. T. Tai, W. H. Chiu, and W. F. Hsieh, Opt. Commun. 245, 301 (2005).

[11]. K. Petermann, IEEE J. Quantum Electron. QE-15, 566 (1979).

[12]. Ashkin, J. M. Dziedzic, J. E. Bjorkholm, and S. Chu, Opt. Lett. 11, 288 (1986).

[13]. P. J. Rodrigo, V. R. Daria, and J. Gluckstad, Opt. Express 12, 1417 (2004).

[14]. J. Arlt, and M. J. Padgett, Opt. Lett. 25, 191 (2000).

簡歷

基本資料

姓名:戴伯澤

性別:男

民國六十五年生於台灣省宜蘭縣

學歷

博士:國立交通大學光電工程研究所 民國 89 年 9 月 ~94 年 6 月

碩士:國立交通大學光電工程研究所 民國 87 年 9 月 ~89 年 6 月

學士:國立中山大學物理系 民國 83 年 9 月 ~87 年 6 月

著作目錄

一、期刊論文

[1]. **P. T. Tai,** H. H. Wu, and W. F. Hsieh**,** "Suppression of spatial hole burning in a solid-state laser with the degenerate resonator configuration," Opt. Express 13, 1679 (2005)

[2]. C. H. Chen, **P. T. Tai**, W. H. Chiu, and W. F. Hsieh, "Transverse excess noise factor and transverse mode locking in a gain-guided laser" Opt. Coumm. 245, 301-308 (2005)

[3]. **P. T. Tai**, C. H. Chen, and W. F. Hsieh, "Direct generation of optical bottle beams from a tightly focused end-pumped solid-state laser," Opt. Express **12**, 5827-5833 (2004)

[4]. C. H. Chen, **P. T. Tai**, and W. F. Hsieh, "Cavity-configuration-dependent instability in a continuously end-pumped solid-state laser," Opt. Coumm. 241, 145-153 (2004)

[5]. C. H. Chen, **P. T. Tai**, and W. F. Hsieh, "Bottle beam from a bare laser for single-beam trapping," Appl. Opt. 43, 6001-6006 (2004)

[6]. C. H. Chen, **P. T. Tai**, W. F. Hsieh, and M. D. Wei, "The multi-beam-waist modes in an end-pumped Nd:YVO4 laser," J. Opt. Soc. Am. B 20, 1220-1226 (2003)

二、會議論文

[1]. "Suppression of spatial hole burning in a standing wave solid-state laser with a degenerate resonator", **P. T. Tai,** H. H. Wu, and W. F. Hsieh**,** APS March Meeting 2005 (has been scheduled for session N13) , Los Angeles, CA, USA (2005).

[2]. "Suppression of spatial hole burning in a standing wave solid-state laser with a degenerate resonator", **P. T. Tai,** H. H. Wu, and W. F. Hsieh, in Conference of Year 2005 Annual Meeting of Chinese Physical Society, Taichung, TAIWAN, paper DF-5 (2005).

[3]. "Direct generation of optical bottle beams from a tightly focused end-pumped solid-state laser", W. H. Chiu, **P. T. Tai**, and W. F. Hsieh, in Conference of Year 2005 Annual Meeting of Chinese Physical Society, Taichung, TAIWAN, paper PE-38 (2005).

[4]. "Single frequency solid state laser operated with multi-beam waist mode under tightly focused axially pumping", **P. T. Tai**, and W. F. Hsieh, in Conference of Year 2004 Annual Meeting of Chinese Physical Society, Taichung, TAIWAN, paper PE-6 (2004).

[5]. "Dynamic of end pump Nd:YVO_4 laser with large pumping spot size around degenerate cavity", G. C. Lee, **P. T. Tai**, C. H. Chen, H. H. Wu, and W. F. Hsieh, in Proceedings of Optics and Photonics Taiwan'03, Taipei, TAIWAN, paper FE1-7 (2003).

[6]. "Observation of multi-beam waist mode due to cooperative frequency locking in a end-pump Nd:YVO_4 laser", **P. T. Tai**, C. H. Chen, H. H. Wu, and W. F. Hsieh, in Proceedings of Optics and Photonics Taiwan'03, Taipei, TAIWAN, paper FE2-2 (2003).

[7]. "Peculiar transverse mode in end-pump Nd:YVO_4 laser", **P. T. Tai**, C. H. Chen and W. F. Hsieh, in Proceedings of Optics and Photonics Taiwan'02, Taipei, TAIWAN, paper TG2-4 (2002).

[8]. "Instabilities due to transverse mode transition in an axially tight-focused solid-state laser", C. H. Chen, **P. T. Tai**, and W. F. Hsieh, in Proceedings of Optics and Photonics Taiwan'02, Taipei, TAIWAN, paper TG2-5 (2002).

[9]. "Dynamics of end pump Nd:YVO_4 laser in degenerate cavity configurations", **P. T. Tai**, W. F. Hsieh, and H. H. Wu, 2nd International Photonics Conference (IPC2000), National Chiao Tung University, Hsinchu, TAIWAN, paper Th-T3-C002, Proc. IPC 2000, pp. 425-428, 2000.